

An SPH formulation for general plate and shell structures with finite deformation and large rotation

Dong Wu^a, Chi Zhang^{a,b}, Xiangyu Hu^{a,*}

^a*TUM School of Engineering and Design, Technical University of Munich, 85748 Garching, Germany*

^b*Huawei Technologies Munich Research Center, 80992 Munich, Germany*

Abstract

In this paper, we propose a reduced-dimensional smoothed particle hydrodynamics (SPH) formulation for quasi-static and dynamic analyses of plate and shell structures undergoing finite deformation and large rotation. By exploiting Uflyand–Mindlin plate theory, the present surface-particle formulation is able to resolve the thin structures by using only one layer of particles at the mid-surface. To resolve the geometric non-linearity and capture finite deformation and large rotation, two reduced-dimensional linear-reproducing correction matrices are introduced, and weighted non-singularity conversions between the rotation angle and pseudo normal are formulated. A new non-isotropic Kelvin-Voigt damping is proposed especially for the both thin and moderately thick plate and shell structures to increase the numerical stability. In addition, a shear-scaled momentum-conserving hourglass control algorithm with an adaptive limiter is introduced to suppress the mismatches between the particle position and pseudo normal and those estimated with

*Corresponding author.

Email addresses: dong.wu@tum.de (Dong Wu), c.zhang@tum.de (Chi Zhang), xiangyu.hu@tum.de (Xiangyu Hu)

the deformation gradient. A comprehensive set of test problems, for which the analytical or numerical results from literature or those of the volume-particle SPH model are available for quantitative and qualitative comparison, are examined to demonstrate the accuracy and stability of the present method.

Keywords: SPH, Uflyand–Mindlin plate theory, Finite deformations, Geometric non-linearity, Thin and moderately thick plate/shell structures, Quasi-static and dynamic analyses, Reduced-dimensional linear-reproducing correction matrices, Non-singularity, Non-isotropic damping, Hourglass modes

1. Introduction

For computational continuum dynamics, as alternatives to conventional mesh-based methods, e.g. finite element method (FEM) and finite volume method (FVM), meshless methods have flourished in the past decades [1, 2, 3, 4]. Smoothed particle hydrodynamics (SPH), initially developed by Lucy [5] and Gingold and Monaghan [6] for astrophysical simulations, is one typical example. In SPH, the continuum is modeled by particles associated with physical properties such as mass and velocity, and the governing equations are discretized in the form of particle interactions using a Gaussian-like kernel function [7, 3, 8]. Since a significant number of physical system abstractions can be realized through particle interactions, SPH has been used to model multi-physical systems within a unified computational framework [9], which is able to achieve seamless monolithic, strong and conservative coupling [10, 11].

To achieve such a unified computational framework, it is crucial to dis-

cretize all relevant physics equations using effective and efficient SPH methods. In the case of plate and shell structures which are omnipresent thin structures in scientific and engineering fields such as shipbuilding [12, 13], aerospace [14], and medical treatment [15], etc., the traditional full-dimensional or volume-particle SPH method, is not computationally efficient [16]. Since there are well-developed and matured reduced-dimensional theories, such as Kirchhoff-Love [17] and Uflyand-Mindlin (or Mindlin-Reissner) [18, 19, 20, 21], for plate and shell structures based on mid-surface reconstruction, it is expected to develop the computationally much more efficient reduced-dimensional or surface-particle SPH method with a single-layer of particles only.

The early meshless methods for plates and shells were based on Petrov or element-free Galerkin formulation [22, 23, 24, 25], or the reproducing kernel particle method [26, 27, 28]. As for SPH, Maurel and Combescure [29] first developed a surface-particle SPH method for total Lagrangian quasi-static and dynamic analyses of moderately thick plates and shells based on the Uflyand-Mindlin theory and the assumption of small deformation. In their work, besides an artificial viscosity term to alleviate numerical instability issues, a stress point method is applied to temper hourglass or zero-energy modes which exhibit in the traditional SPH method using collocated particles for both deformation and stress. While being effective on preventing zero-energy modes, using stress points may faces several issues, such as how to locate or generate these points for complex geometries, complicated numerical algorithms and the compensation of computational efficiency [30, 31]. Nevertheless, this method was later applied in large deformation analyses by

Ming et al. [32] and dynamic damage-fracture analyses by Caleyron et al. [33]. Lin et al. [34] developed a similar method for quasi-static analyses, but applied an artificial viscosity term based on membrane and shearing decomposition. Ming et al. [35] first considered finite deformation by taking all strain terms into account with the help of Gauss-Legendre quadrature for more accurately capturing of non-linear stress. In all of the surface-particle SPH methods mentioned above, the rotation angles of mid-surface are directly obtained from the pseudo normal in governing equations under the assumption of small rotation.

In this work, we propose a collocated surface-particle SPH formulation for total Lagrangian quasi-static and dynamic analyses of general plate or shell structures, which may be thin or have moderate thickness, involving finite deformation or/and large rotation. First, to better resolve the geometric non-linearity induced by finite deformation and large rotation, two new reduced-dimensional correction matrices for linearly reproducing position and normal direction are introduced, and a weighted conversion algorithm, which achieves non-singularity under large rotation, is proposed. Second, a new non-isotropic Kelvin-Voigt damping base on Ref. [36] is proposed for achieve good numerical stability for both thin and moderately thick plate or shell structures. Third, in order to address hourglass modes using collocated particles only other than introducing extra stress points, drawing the inspiration from Refs. [37, 30], a shear-scaled momentum-conserving formulation with an adaptive limiter is developed by mitigating the discrepancy between the actual particle position and pseudo normal and those estimated by the deformation gradient. A set of numerical examples involving quasi-static and

dynamic analyses for both thin and moderately thick plate or shell structures are given. The results are compared with analytical, numerical solutions in literature or/and those obtained by the volume-particle SPH method to demonstrate the numerical accuracy and stability of the present method.

The remainder of this manuscript is organized as follows. Section 2 introduces the theoretical model of plates and shells, including the kinematics, constitutive relation, stress correction and conservation equations. The proposed surface-particle SPH formulation, including the reduced-dimensional linear-producing correction matrices, weighted conversion algorithm, non-isotropic damping and momentum-conserving hourglass control, is described in Section 3. Numerical examples are presented and discussed in Section 4 and then concluding remarks are given in Section 5. For a better comparison and future opening for in-depth studies, all the computational codes of this work are released in the open-source repository of SPHinXsys [38, 9] at <https://github.com/Xiangyu-Hu/SPHinXsys>.

2. Theoretical models

We first introduce the theoretical mode of 3D plate, and then that of 3D shell in which material points may possess different initial normal directions leading to different initial local coordinate systems. After that, we briefly describe the 2D plate and shell models, which resolve the plane strain problem, as a simplification of the 3D counterparts.

2.1. 3D plate model

We consider the Uflyand–Mindlin plate theory [18, 19] to account for transverse shear stress which is significant for moderately thick plates. The

theory implies that the plate behavior can be represented by one layer of material points at its mid-surface, as shown in Figure 1.

2.1.1. Kinematics

We introduce $\mathbf{X} = (X, Y, Z)$ to represent the global coordinate system, and $\boldsymbol{\xi} = (\xi, \eta, \zeta)$ and $\mathbf{x} = (x, y, z)$, associated with so-called pseudo-normal vector \mathbf{n} , to denote the initial and current local coordinate systems, respectively. Note that the initial local coordinate system is same with the global one for plate. Each material point possesses five degrees of freedom, viz., three translations $\mathbf{u} = \{u, v, w\}^T$ and two rotations $\boldsymbol{\theta} = \{\theta, \varphi\}^T$ expressed in the global coordinates. Positive values of θ and φ indicate that the plate is rotated anticlockwise around the coordinate axis when the axis points toward the observer and the coordinate system is right-handed. The two rotations are used to update the pseudo-normal $\mathbf{n} = \{n_1, n_2, n_3\}^T$ which is also defined in the global coordinate system and remains straight but is not necessarily perpendicular to the mid-surface, i.e., the pseudo normal may be different with the real normal \mathbf{n}_r , as shown in Figure 1. Note that $\mathbf{n}^0 = \{0, 0, 1\}^T$ denotes the pseudo-normal in the initial configuration with the superscript $(\bullet)^0$ denoting the initial configuration.

For a 3D plate, the position \mathbf{r} of a material point at a distance χ away from the mid-surface along the pseudo normal \mathbf{n} can be expressed as

$$\mathbf{r}(\xi, \eta, \chi, t) = \mathbf{r}_m(\xi, \eta, t) + \chi \mathbf{n}(\xi, \eta, t), \quad \chi \in [-d/2, d/2], \quad (1)$$

where d is the thickness, \mathbf{r}_m the position of the material point at the mid-surface with the subscript $(\bullet)_m$ denoting the mid-surface. Note that since the thickness is assumed to be constant during deformation and the pseudo

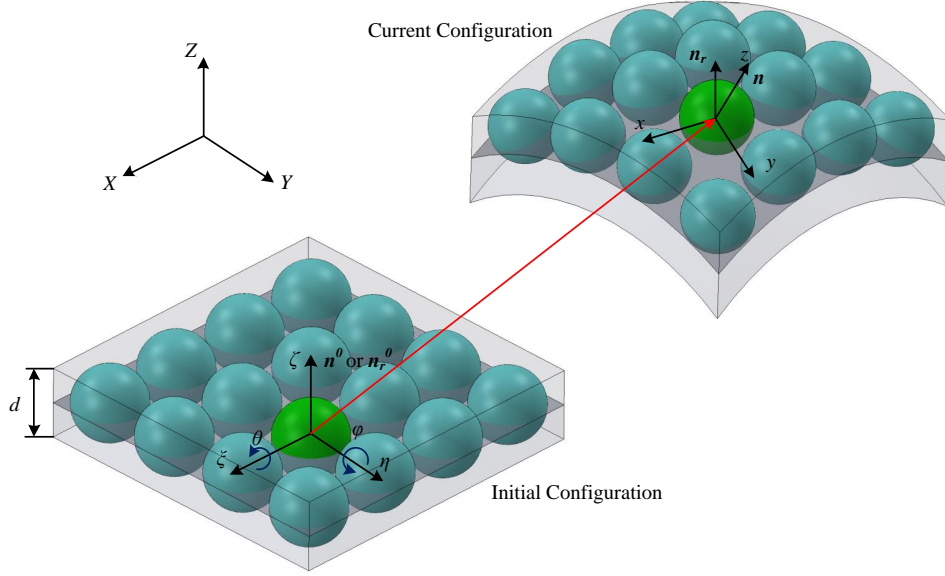


Figure 1: Schematic of a 3D plate model.

normal \mathbf{n} represents the plate thickness direction, the distance χ is always between $-d/2$ and $d/2$. Therefore, the displacement \mathbf{u} of the material point can be determined by

$$\mathbf{u}(\xi, \eta, \chi, t) = \mathbf{u}_m(\xi, \eta, t) + \chi \Delta \mathbf{n}(\xi, \eta, t), \quad (2)$$

where $\Delta \mathbf{n} = \mathbf{n} - \mathbf{n}^0$. Then we can define the deformation gradient tensor as

$$\mathbb{F} = \nabla^0 \mathbf{r} = \nabla^0 \mathbf{u} + \mathbb{I} = (\mathbf{a}_1, \mathbf{a}_2, \mathbf{a}_3), \quad (3)$$

where $\nabla^0 \equiv \partial/\partial \boldsymbol{\xi}$ is the gradient operator with respect to the initial configuration, \mathbb{I} the identity matrix, and $\mathbf{a}_1, \mathbf{a}_2, \mathbf{a}_3$ are specified by

$$\begin{cases} \mathbf{a}_1 = \mathbf{r}_{m,\xi} + \chi \mathbf{n}_\xi \\ \mathbf{a}_2 = \mathbf{r}_{m,\eta} + \chi \mathbf{n}_\eta \\ \mathbf{a}_3 = \mathbf{n} \end{cases} \quad (4)$$

with $\nabla^0 \mathbf{r}_m \equiv (\mathbf{r}_{m,\xi}, \mathbf{r}_{m,\eta})^\top$ and $\nabla^0 \mathbf{n} \equiv (\mathbf{n}_\xi, \mathbf{n}_\eta)^\top$. The deformation gradient tensor can be decomposed into two components as

$$\mathbb{F} = \mathbb{F}_m + \chi \mathbb{F}_n, \quad (5)$$

where $\mathbb{F}_m = (\mathbf{r}_{m,\xi}^\top, \mathbf{r}_{m,\eta}^\top, \mathbf{n}^\top)$ and $\mathbb{F}_n = (\mathbf{n}_\xi^\top, \mathbf{n}_\eta^\top, 0)$. Furthermore, the real normal \mathbf{n}_r is given as

$$\mathbf{n}_r = \frac{\mathbf{r}_{m,\xi} \times \mathbf{r}_{m,\eta}}{|\mathbf{r}_{m,\xi} \times \mathbf{r}_{m,\eta}|}. \quad (6)$$

2.1.2. Constitutive relation

With the deformation gradient tensor \mathbb{F} , the Green-Lagrangian strain tensor \mathbb{E} can be obtained as

$$\mathbb{E} = \frac{1}{2} (\mathbb{F}^\top \mathbb{F} - \mathbb{I}) = \frac{1}{2} (\mathbb{C} - \mathbb{I}), \quad (7)$$

where \mathbb{C} is the right Cauchy deformation gradient tensor. The Eulerian Almansi strain ϵ can be converted from \mathbb{E} as

$$\epsilon = \mathbb{F}^{-\top} \cdot \mathbb{E} \cdot \mathbb{F}^{-1} = \frac{1}{2} (\mathbb{I} - \mathbb{F}^{-\top} \mathbb{F}^{-1}). \quad (8)$$

When the material is linear and isotropic, the Cauchy stress σ reads

$$\begin{aligned} \sigma &= K \operatorname{tr}(\epsilon) \mathbb{I} + 2G \left(\epsilon - \frac{1}{3} \operatorname{tr}(\epsilon) \mathbb{I} \right) \\ &= \lambda \operatorname{tr}(\epsilon) \mathbb{I} + 2\mu \epsilon, \end{aligned} \quad (9)$$

where λ and μ are the Lamé constants, $K = \lambda + 2\mu/3$ the bulk modulus and $G = \mu$ the shear modulus. The relationship between the two moduli is given by

$$E = 2G(1 + \nu) = 3K(1 - 2\nu), \quad (10)$$

where E denotes the Young's modulus and ν the Poisson's ratio.

2.1.3. Stress correction

As the thickness is significantly less than the length and width of plate, the following boundary conditions hold when the plate is free from external forces on its surfaces where $\chi = \pm \frac{d}{2}$ or $z = \pm \frac{d}{2}$

$$\sigma_{xz}^l \Big|_{z=\pm \frac{d}{2}} = 0, \quad \sigma_{yz}^l \Big|_{z=\pm \frac{d}{2}} = 0, \quad (11)$$

$$\sigma_{zz}^l \Big|_{z \in [-\frac{d}{2}, \frac{d}{2}]} = 0, \quad (12)$$

with the superscript $(\bullet)^l$ denoting the current local coordinates. Taking the boundary condition Eq. (12) and constitutive Eq. (9) into account, the following relation of strains holds [26]

$$\epsilon_{zz}^l = \frac{-\nu (\epsilon_{xx}^l + \epsilon_{yy}^l)}{1 - \nu}, \quad (13)$$

where the current local strain ϵ^l is obtained by

$$\epsilon^l = \mathbb{Q} \epsilon \mathbb{Q}^T. \quad (14)$$

Here, \mathbb{Q} is the orthogonal transformation matrix from the global to current local coordinates. Following Batoz and Dhatt [39], \mathbb{Q} can be given as

$$\mathbb{Q} = \begin{bmatrix} n_3 + \frac{(n_2)^2}{1+n_3} & -\frac{n_1 n_2}{1+n_3} & -n_1 \\ -\frac{n_1 n_2}{1+n_3} & n_3 + \frac{(n_1)^2}{1+n_3} & -n_2 \\ n_1 & n_2 & n_3 \end{bmatrix}. \quad (15)$$

To satisfy the boundary conditions of Eq. (11), the transverse shear stress should be corrected as [40]

$$\bar{\sigma}_{xz}^l = \bar{\sigma}_{zx}^l = \kappa \sigma_{xz}^l, \quad \bar{\sigma}_{yz}^l = \bar{\sigma}_{zy}^l = \kappa \sigma_{yz}^l, \quad (16)$$

where κ denotes the shear correction factor which is typically set to 5/6 for the rectangular section of the isotropic plate. Taking the corrected strain $\bar{\boldsymbol{\epsilon}}^l$ into constitutive Eq. (9) and then applying Eq. (16), the corrected current local Cauchy stress $\bar{\boldsymbol{\sigma}}^l$ is obtained.

2.1.4. Conservation equations

The mass conservation equation can be written as

$$\rho = J_m^{-1} \rho^0, \quad (17)$$

where $J_m = \det(\mathbb{F}_m)$, ρ^0 and ρ represent the initial and current densities, respectively. The momentum conservation equation is

$$\rho \ddot{\mathbf{u}}^l = \nabla \cdot (\bar{\boldsymbol{\sigma}}^l)^T \quad (18)$$

or

$$\rho \begin{bmatrix} \ddot{u}^l \\ \ddot{v}^l \\ \ddot{w}^l \end{bmatrix} = \begin{bmatrix} \frac{\partial \bar{\sigma}_{xx}^l}{\partial x} + \frac{\partial \bar{\sigma}_{xy}^l}{\partial y} + \frac{\partial \bar{\sigma}_{xz}^l}{\partial z} \\ \frac{\partial \bar{\sigma}_{yx}^l}{\partial x} + \frac{\partial \bar{\sigma}_{yy}^l}{\partial y} + \frac{\partial \bar{\sigma}_{yz}^l}{\partial z} \\ \frac{\partial \bar{\sigma}_{zx}^l}{\partial x} + \frac{\partial \bar{\sigma}_{zy}^l}{\partial y} + \frac{\partial \bar{\sigma}_{zz}^l}{\partial z} \end{bmatrix}. \quad (19)$$

With Eqs. (11) and (12), we can integrate Eq. (19) along χ or $z \in [-d/2, d/2]$

as

$$d\rho \begin{bmatrix} \ddot{u}_m^l \\ \ddot{v}_m^l \\ \ddot{w}_m^l \end{bmatrix} = \begin{bmatrix} \frac{\partial N_{xx}^l}{\partial x} + \frac{\partial N_{xy}^l}{\partial y} \\ \frac{\partial N_{yx}^l}{\partial x} + \frac{\partial N_{yy}^l}{\partial y} \\ \frac{\partial N_{zx}^l}{\partial x} + \frac{\partial N_{zy}^l}{\partial y} \end{bmatrix}, \quad (20)$$

where the stress resultant \mathbb{N}^l is calculated by the Gauss–Legendre quadrature rule as

$$\mathbb{N}^l = \int_{-d/2}^{d/2} \bar{\boldsymbol{\sigma}}^l(z) dz = \sum_{ip=1}^N \bar{\boldsymbol{\sigma}}^l(z_{ip}) A_{ip}. \quad (21)$$

Here, z_{ip} is the integral point, A_{ip} the weight, and N the number of the integral point. Since the quadrature rule is conducted to yield an exact result for polynomials of degree $2N - 1$ or lower [41], N is determined by the applied constitutive relation.

By multiplying both sides of Eq. (18) by z and integrating along $z \in [-d/2, d/2]$, the angular momentum conservation equation can be obtained as

$$\frac{d^3}{12}\rho \begin{bmatrix} \ddot{n}_1^l \\ \ddot{n}_2^l \\ \ddot{n}_3^l \end{bmatrix} = \begin{bmatrix} \frac{\partial M_{xx}^l}{\partial x} + \frac{\partial M_{xy}^l}{\partial y} \\ \frac{\partial M_{yx}^l}{\partial x} + \frac{\partial M_{yy}^l}{\partial y} \\ \frac{\partial M_{zx}^l}{\partial x} + \frac{\partial M_{zy}^l}{\partial y} \end{bmatrix} + \begin{bmatrix} -N_{xz}^l \\ -N_{yz}^l \\ 0 \end{bmatrix}, \quad (22)$$

where the moment resultant \mathbb{M}^l is calculated as

$$\mathbb{M}^l = \int_{-d/2}^{d/2} z \bar{\sigma}^l(z) dz = \sum_{ip=1}^N z_{ip} \bar{\sigma}^l(z_{ip}) A_{ip}. \quad (23)$$

Note that

$$\int_{-d/2}^{d/2} z \frac{\partial \bar{\sigma}_{xz}^l}{\partial z} dz = \left[z \bar{\sigma}_{xz}^l \right]_{-d/2}^{d/2} - \int_{-d/2}^{d/2} \bar{\sigma}_{xz}^l dz = -N_{xz}^l. \quad (24)$$

Therefore, the two governing equations, including the evolution of mid-surface displacement and pseudo normal, respectively, for the 3D plate can be described as

$$\begin{cases} d\rho \ddot{\mathbf{u}}_m^l = \nabla^l \cdot (\mathbb{N}^l)^\top \\ \frac{d^3}{12} \rho \ddot{\mathbf{n}}^l = \nabla^l \cdot (\mathbb{M}^l)^\top + \mathbf{Q}^l, \end{cases} \quad (25)$$

where

$$\mathbb{N}^l = \begin{bmatrix} N_{xx}^l & N_{xy}^l & 0 \\ N_{yx}^l & N_{yy}^l & 0 \\ N_{zx}^l & N_{zy}^l & 0 \end{bmatrix}, \mathbb{M}^l = \begin{bmatrix} M_{xx}^l & M_{xy}^l & 0 \\ M_{yx}^l & M_{yy}^l & 0 \\ M_{zx}^l & M_{zy}^l & 0 \end{bmatrix}, \mathbf{Q}^l = \begin{bmatrix} -N_{xz}^l \\ -N_{yz}^l \\ 0 \end{bmatrix}. \quad (26)$$

In total Lagrangian formulation, the conservation equations above are converted into

$$\begin{cases} d\rho^0 \dot{\mathbf{u}}_m = (\mathbb{F}_m)^{-\text{T}} \nabla^0 \cdot (J_m \mathbb{N}^{\text{T}}) \\ \frac{d^3}{12} \rho^0 \dot{\mathbf{n}} = (\mathbb{F}_m)^{-\text{T}} \nabla^0 \cdot (J_m \mathbb{M}^{\text{T}}) + J_m \mathbb{Q}^{\text{T}} \mathbb{Q}^l, \end{cases} \quad (27)$$

where $\mathbb{N} = \mathbb{Q}^{\text{T}} \mathbb{N}^l \mathbb{Q}$ and $\mathbb{M} = \mathbb{Q}^{\text{T}} \mathbb{M}^l \mathbb{Q}$ are the stress and moment resultants, respectively, in global coordinates.

2.2. 3D shell model

Based on the 3D plate model, the 3D shell model is obtained by introducing the initial local coordinate system and the transformation matrix from the global to initial local coordinate system.

2.2.1. Kinematics

The kinematics of shell can be constructed in the initial local coordinates denoted with the superscript $(\bullet)^L$. Each material point possesses five degrees of freedom, viz., three translations $\mathbf{u}^L = \{u^L, v^L, w^L\}^{\text{T}}$ and two rotations $\boldsymbol{\theta}^L = \{\theta^L, \varphi^L\}^{\text{T}}$ as shown in Figure 2. The pseudo-normal vector is also presented in initial local coordinates by $\mathbf{n}^L = \{n_1^L, n_2^L, n_3^L\}^{\text{T}}$, especially denoted by $\mathbf{n}^{0,L} = \{0, 0, 1\}^{\text{T}}$ in the initial local configuration. The local position \mathbf{r}^L of a material point can be expressed as

$$\mathbf{r}^L(\xi, \eta, \chi, t) = \mathbf{r}_m^L(\xi, \eta, t) + \chi \mathbf{n}^L(\xi, \eta, t), \quad \chi \in [-d/2, d/2]. \quad (28)$$

The local displacement \mathbf{u}^L can thus be obtained by

$$\mathbf{u}^L(\xi, \eta, \chi, t) = \mathbf{u}_m^L(\xi, \eta, t) + \chi \Delta \mathbf{n}^L(\xi, \eta, t), \quad (29)$$

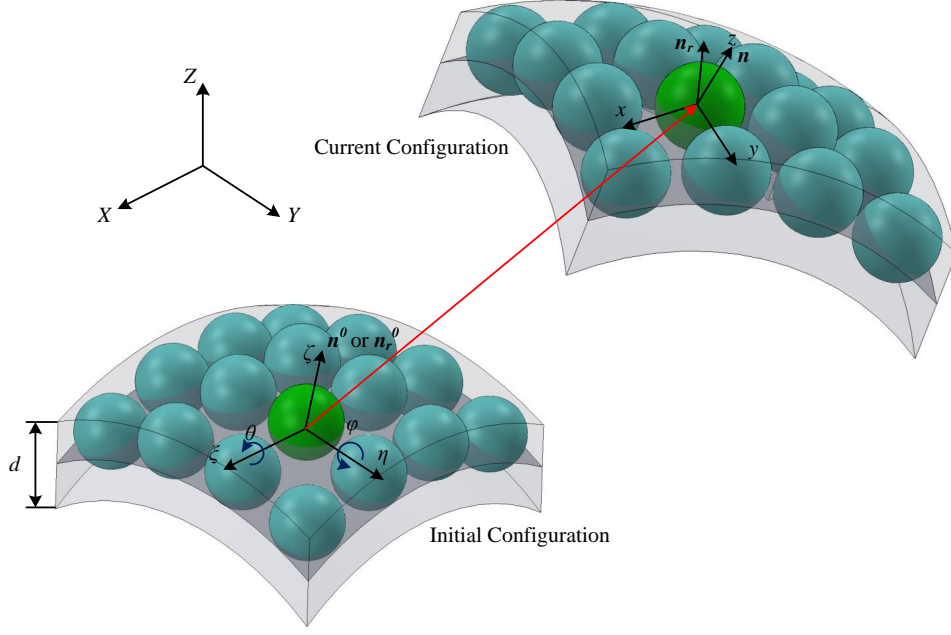


Figure 2: Schematic of a 3D shell model.

where $\Delta \mathbf{n}^L = \mathbf{n}^L - \mathbf{n}^{0,L}$. Similar to 3D plates, the local deformation gradient tensor of 3D shells can be defined as

$$\mathbb{F}^L = \nabla^{0,L} \mathbf{r}^L + \nabla^{0,L} \mathbf{n}^L - \nabla^{0,L} \mathbf{n}^{0,L} = (\mathbf{a}_1^L, \mathbf{a}_2^L, \mathbf{a}_3^L), \quad (30)$$

where $\nabla^{0,L} \equiv \partial/\partial \boldsymbol{\xi}$ is the gradient operators defined in the initial local configuration, and $\mathbf{a}_1^L, \mathbf{a}_2^L, \mathbf{a}_3^L$ are detailed by

$$\begin{cases} \mathbf{a}_1^L = \mathbf{r}_{m,\xi}^L + \chi \mathbf{n}_\xi^L - \chi \mathbf{n}_\xi^{0,L} \\ \mathbf{a}_2^L = \mathbf{r}_{m,\eta}^L + \chi \mathbf{n}_\eta^L - \chi \mathbf{n}_\eta^{0,L} \\ \mathbf{a}_3^L = \mathbf{n}^L. \end{cases} \quad (31)$$

2.2.2. Stress correction and conservation equation

With the local deformation gradient tensor \mathbb{F}^L , the local Eulerian Almansi strain $\boldsymbol{\epsilon}^L$ can be calculated by the Eq. (8). After that, the current local $\boldsymbol{\epsilon}^l$ is

obtained according to the coordinate transformation as

$$\bar{\boldsymbol{\epsilon}}^l = \mathbb{Q} (\mathbb{Q}^0)^T \boldsymbol{\epsilon}^L \mathbb{Q}^0 \mathbb{Q}^T, \quad (32)$$

where \mathbb{Q}^0 , the orthogonal transformation matrix from the global to initial local coordinates, is calculated from Eq. (15) while the current pseudo normal \mathbf{n} is replaced by the initial one \mathbf{n}^0 . And then the corrected strain $\bar{\boldsymbol{\epsilon}}^l$ is estimated by applying Eq. (13). After getting the current local Cauchy stress $\boldsymbol{\sigma}^l$ by Eq. (9), the corrected one $\bar{\boldsymbol{\sigma}}^l$ is obtained by Eq. (16).

Note that the total Lagrangian conservation equations of a 3D shell has the same form as Eqs. (27) with $\mathbb{F}_m = (\mathbb{Q}^0)^T \mathbb{F}_m^L \mathbb{Q}^0$.

2.3. 2D plate/shell model

If a plate/shell is assumed to be a strip that is very long and has a finite width, and the transverse load is assumed to be uniform along the length, the analysis can be simplified at any cross section as a plane strain problem [42].

The kinematics of 2D plate and shell can all be built in initial local coordinates, as the transformation matrix \mathbb{Q}^0 from the global to initial local coordinates for the plate is the unit matrix. The 2D model is in the global X - Z plane, and each material point possesses three degrees of freedom, viz., two translations $\mathbf{u}^L = \{u^L, w^L\}^T$ and one rotation $\boldsymbol{\theta}^L = \{\varphi^L\}^T$ expressed in the initial local coordinates. The pseudo-normal vector is presented in the initial local coordinates by $\mathbf{n}^L = \{n_1^L, n_3^L\}^T$, especially denoted by $\mathbf{n}^{0,L} = \{0, 1\}^T$ in the initial local configuration. Similar to 3D model, the local position \mathbf{r}^L of a material point can be expressed as

$$\mathbf{r}^L(\xi, \chi, t) = \mathbf{r}_m^L(\xi, t) + \chi \mathbf{n}^L(\xi, t), \quad \chi \in [-d/2, d/2], \quad (33)$$

the local displacement \mathbf{u}^L can be evaluated as

$$\mathbf{u}^L(\xi, \chi, t) = \mathbf{u}_m^L(\xi, t) + \chi \Delta \mathbf{n}^L(\xi, t). \quad (34)$$

and the local deformation gradient tensor is written as

$$\mathbb{F}^L = \nabla^{0,L} \mathbf{r}^L + \nabla^{0,L} \mathbf{n}^L - \nabla^{0,L} \mathbf{n}^{0,L} = (\mathbf{a}_1^L, \mathbf{a}_3^L), \quad (35)$$

where \mathbf{a}_1^L and \mathbf{a}_3^L are given by

$$\begin{cases} \mathbf{a}_1^L = \mathbf{r}_{m,\xi}^L + \zeta \mathbf{n}_\xi^L - \zeta \mathbf{n}_\xi^{0,L} \\ \mathbf{a}_3^L = \mathbf{n}^L. \end{cases} \quad (36)$$

The coordinate transformation matrix \mathbb{Q} from global to current local coordinates is simplified from Eqs. (15) as

$$\mathbb{Q} = \begin{bmatrix} n_3 & -n_1 \\ n_1 & n_3 \end{bmatrix}, \quad (37)$$

and the 2D transformation matrix \mathbb{Q}^0 from global to initial local coordinates can also be calculated by Eq. (37) while the current pseudo normal \mathbf{n} is replaced by the initial one \mathbf{n}^0 . The corrected relation of strains is simplified from Eq. (13) as

$$\bar{\epsilon}_{zz}^l = \frac{-\nu \epsilon_{xx}^l}{1 - \nu}. \quad (38)$$

Finally, the 2D conservation equation is identical to 3D Eq. (27) with

$$\mathbb{N}^l = \begin{bmatrix} N_{xx}^l & 0 \\ N_{zx}^l & 0 \end{bmatrix}, \mathbb{M}^l = \begin{bmatrix} M_{xx}^l & 0 \\ M_{zx}^l & 0 \end{bmatrix}, \mathbb{Q}^l = \begin{bmatrix} -N_{xz}^l \\ 0 \end{bmatrix}. \quad (39)$$

3. SPH method for plate and shell structures

In this section, we first introduce the reduced-dimensional SPH method, and detail the proposed formulations for plate and shell structures, including the discretization of conservation equations, non-singular conversion algorithm for the kinematics between rotation angles and pseudo normal, and the algorithms to increase numerical stability and alleviate hourglass modes. After that, the time-integration schemes are presented.

3.1. Reduced-dimensional SPH method

In full-dimensional SPH method, the smoothed field $f(\mathbf{r})$ is obtained as

$$f(\mathbf{r}) = \int_{\Omega} f(\mathbf{r}') W(\mathbf{r} - \mathbf{r}', h) d\mathbf{r}', \quad (40)$$

where $f(\mathbf{r}')$ is the original continuous field before smoothing, Ω the entire space and $W(\mathbf{r} - \mathbf{r}', h)$ a Gaussian-like kernel function with smoothing length h denoting the compact support. By carrying out the integration of Eq. (40) along the thickness of the plate/shell structure, we can obtain the reduced-dimensional smoothed field by

$$f(\mathbf{r}) \approx \int_{\widehat{\Omega}} f(\mathbf{r}') \widehat{W}(\mathbf{r} - \mathbf{r}', h) d\mathbf{r}', \quad (41)$$

where $\widehat{\Omega}$ denotes the reduced space and $\widehat{W}(\mathbf{r} - \mathbf{r}', h)$ the reduced kernel function. Note that Eqs. (40) and (41) have identical forms of formulation. A reduced-dimensional fifth-order Wendland kernel [43] reads

$$\widehat{W}(q, h) = \alpha \begin{cases} (1 + 2q)(1 - q/2)^4 & \text{if } 0 \leq q \leq 2 \\ 0 & \text{otherwise} \end{cases}, \quad (42)$$

where $q = |\mathbf{r} - \mathbf{r}'|/h$ and the constant α is equal to $\frac{3}{4h}$ and $\frac{7}{4\pi h^2}$ for 2D and 3D problems, respectively. Also note that the reduced kernel function has identical form with the full-dimensional counterpart except different dimensional normalizing constant parameter, allowing the integration of unit can be satisfied in the reduced space. Due to the almost identical forms, in present work from here, we do not identify the full- and reduced-dimensional formulations unless explicitly mentioned.

In the reduced-dimensional SPH method, similarly to the full-dimensional counterpart [7], the gradient of the variable field $f(\mathbf{r})$ at a surface particle i can be approximated as

$$\begin{aligned}\nabla f_i &= \int_{\Omega} \nabla f(\mathbf{r}) W(\mathbf{r}_i - \mathbf{r}, h) d\mathbf{r} \\ &= - \int_{\Omega} f(\mathbf{r}) \nabla W(\mathbf{r}_i - \mathbf{r}, h) d\mathbf{r} \approx - \sum_j f_j \nabla W_{ij} V_j,\end{aligned}\tag{43}$$

where V is the reduced particle volume, i.e. length and area for 2D and 3D problems, respectively. Here, the summation is conducted over all the neighboring particles j located at the support domain of the particle i , and $\nabla W_{ij} = -\frac{\partial W(\mathbf{r}_{ij}, h)}{\partial \mathbf{r}_{ij}} \mathbf{e}_{ij}$ is the gradient of the kernel function with $\mathbf{r}_{ij} = \mathbf{r}_i - \mathbf{r}_j$ and $\mathbf{e}_{ij} = \mathbf{r}_{ij}/|\mathbf{r}_{ij}|$ denoting the unit vector pointing from particle j to i . Equation (43) can be modified into a strong form as

$$\nabla f_i = \nabla f_i - f_i \nabla 1 \approx \sum_j f_{ij} \nabla W_{ij} V_j,\tag{44}$$

where $f_{ij} = f_i - f_j$ is the interparticle difference value. This strong-form derivative operator can be used to determine the local structure of a field, such as the deformation gradient tensor. And Eq. (43) can also be modified

into a weak form as

$$\nabla f_i = f_i \nabla 1 + \nabla f_i \approx - \sum_j (f_i + f_j) \nabla W_{ij} V_j. \quad (45)$$

This weak-form derivative operator is applied here for solving the conservation equations. Thanks to its anti-symmetric feature, i.e., $\nabla W_{ij} = -\nabla W_{ji}$, the momentum conservation of the particle system is ensured [7].

Also note that, in the present work, the reduced-dimensional SPH method is employed for total Lagrangian formulation [44], such as Eq. (27). Therefore, the smoothing kernel function and its derivatives are only evaluated once, also denoted with superscript $(\bullet)^0$ at the initial configuration, and kept unchanged during the simulation.

3.2. First-order consistency corrections

For the full-dimensional SPH in total Lagrangian formulation, in order to remedy the 1st-order inconsistency which is caused by incomplete kernel support at domain boundary or with irregular particle distribution, the symmetric correction matrix \mathbb{B}_i^0 for each particle [45, 3] is introduced for each particle to satisfy the linear-reproducing condition

$$\left(\sum_j \mathbf{r}_{ij}^0 \otimes \nabla^0 W_{ij} V_j^0 \right) \mathbb{B}_i^0 = \mathbb{I}. \quad (46)$$

Then the strong-form approximations of gradient Eq. (44) is modified as

$$\nabla^0 f_i \approx \left(\sum_j f_{ij} \nabla^0 W_{ij} V_j^0 \right) \mathbb{B}_i^0, \quad (47)$$

and the weak-form approximations of divergence Eq. (45) as

$$\nabla^0 \cdot f_i \approx - \sum_j (f_i \mathbb{B}_i^0 + f_j \mathbb{B}_j^0) \nabla^0 W_{ij} V_j^0. \quad (48)$$

In the reduced-dimensional SPH, we generalize the linear-reproducing condition as

$$\left[\mathbb{G}^T \mathbb{Q}_i^0 \left(\sum_j \mathbf{q}_{ij}^0 \otimes \nabla^0 W_{ij} V_j^0 \right) (\mathbb{Q}_i^0)^T \mathbb{G} \right] \mathbb{B}_i^{0,L} = \mathbb{K}_i, \quad (49)$$

where \mathbf{q}_{ij}^0 is the initial inter-particle difference of a linear vector, \mathbb{Q}_i^0 is the transformation matrix from the global to initial local coordinates, and \mathbb{G} is a reducing matrix, i.e.,

$$\mathbb{G} = \begin{bmatrix} 1 \\ 0 \end{bmatrix} \quad \text{and} \quad \begin{bmatrix} 1 & 0 \\ 0 & 1 \\ 0 & 0 \end{bmatrix} \quad (50)$$

for 2D and 3D problems, respectively. It ensures that the corrections are carried out within the local reduced space. Similarly, the strong-form approximations of gradient Eq. (44) is modified as

$$\nabla^0 f_i \approx \left(\sum_j f_{ij} \nabla^0 W_{ij} V_j^0 \right) \tilde{\mathbb{B}}_i^0, \quad (51)$$

where $\tilde{\mathbb{B}}_i^0 = (\mathbb{Q}_i^0)^T \mathbb{G} \mathbb{B}_i^{0,L} \mathbb{G}^T \mathbb{Q}_i^0$ and the weak-form approximations of divergence Eq. (45) as

$$\nabla^0 \cdot f_i \approx - \sum_j \left(f_i \tilde{\mathbb{B}}_i^0 + f_j \tilde{\mathbb{B}}_j^0 \right) \nabla^0 W_{ij} V_j^0. \quad (52)$$

Here, we introduce the correction matrix $\tilde{\mathbb{B}}_i^0 = \tilde{\mathbb{B}}_i^{0,r}$, $\mathbf{q}_{ij}^0 = \mathbf{r}_{ij}^0$ and \mathbb{K}_i is the reduced identity matrix denoted as

$$\mathbb{K}_i = \mathbb{K}^r = \begin{bmatrix} 1 \\ 1 \end{bmatrix} \quad \text{and} \quad \begin{bmatrix} 1 & 0 \\ 0 & 1 \end{bmatrix} \quad (53)$$

for 2D and 3D problems, respectively, to correct the position-based quantities. Similarly, we introduce the correction matrix $\tilde{\mathbb{B}}_i^0 = \tilde{\mathbb{B}}_i^{0,\mathbf{n}}$, $\mathbf{q}_{ij}^0 = \mathbf{n}_{ij}^0$ and

$$\mathbb{K}_i = \mathbb{K}_i^{\mathbf{n}} = \left[1/R_i^L \right] \text{ and } \begin{bmatrix} 1/R_{1,i}^L & 0 \\ 0 & 1/R_{2,i}^L \end{bmatrix}, \quad (54)$$

where R_i^L , $R_{1,i}^L$ and $R_{2,i}^L$ are the curvature radii of particle i for 2D and 3D problems, respectively, to correct rotation-based quantities.

3.3. Discretization of conservation equations

With two correction matrices obtained from Eq. (49) and following Eq. (52), the momentum equations (27) are discretized as

$$d\rho_i^0 \dot{\mathbf{u}}_{m,i} = \sum_j \left(J_{m,i} \mathbb{N}_i (\mathbb{F}_{m,i})^{-\text{T}} \tilde{\mathbb{B}}_i^{0,\mathbf{r}} + J_{m,j} \mathbb{N}_j (\mathbb{F}_{m,j})^{-\text{T}} \tilde{\mathbb{B}}_j^{0,\mathbf{r}} \right) \nabla^0 W_{ij} V_j^0, \quad (55)$$

and

$$\begin{aligned} \frac{d^3}{12} \rho_i^0 \ddot{\mathbf{n}}_i &= \sum_j \left(J_{m,i} \mathbb{M}_i (\mathbb{F}_{m,i})^{-\text{T}} \tilde{\mathbb{B}}_i^{0,\mathbf{n}} + J_{m,j} \mathbb{M}_j (\mathbb{F}_{m,j})^{-\text{T}} \tilde{\mathbb{B}}_j^{0,\mathbf{n}} \right) \nabla^0 W_{ij} V_j^0 \\ &+ J_{m,i} (\mathbb{Q}_i^0)^{\text{T}} \mathbf{Q}_i^l. \end{aligned} \quad (56)$$

3.4. Kelvin–Voigt type damping

Following Ref. [36], when calculating the current local Cauchy stress by using the constitutive Eq. (9), an artificial damping stress σ_d^l based on the Kelvin–Voigt type damper is introduced here as

$$\sigma_d^l = J_m^{-1} \mathbb{Q} (\mathbb{Q}^0)^{\text{T}} \mathbb{F}^L \dot{\mathbb{E}}^L \gamma (\mathbb{F}^L)^{\text{T}} \mathbb{Q}^0 \mathbb{Q}^{\text{T}}, \quad (57)$$

where the numerical viscosity matrix

$$\gamma = \begin{bmatrix} \rho ch/2 & 0 \\ 0 & \rho cs/2 \end{bmatrix} \text{ and } \begin{bmatrix} \rho ch/2 & 0 & 0 \\ 0 & \rho ch/2 & 0 \\ 0 & 0 & \rho cs/2 \end{bmatrix} \quad (58)$$

where $c = \sqrt{K/\rho}$ and $s = \min(h, d)$, for 2D and 3D problems, respectively. Note that, different from Ref. [36], where an isotropic numerical damping is applied, the present damping leads to a smaller out-of-plane contribution when $d \leq h$, which makes it suitable for both thin and moderately thick plate and shell structures. The change rate of the Green-Lagrangian strain tensor is given as

$$\dot{\mathbb{E}}^L = \frac{1}{2} \left[\left(\dot{\mathbb{F}}^L \right)^T \mathbb{F}^L + \left(\mathbb{F}^L \right)^T \dot{\mathbb{F}}^L \right]. \quad (59)$$

Here, the change rate of the deformation gradient tensor of particle i is

$$\dot{\mathbb{F}}_i^L = \nabla^{0,L} \dot{\mathbf{u}}_i^L = \nabla^0 \dot{\mathbf{u}}_{m,i}^L + \chi \nabla^0 \dot{\mathbf{n}}_i^L, \quad (60)$$

where

$$\begin{cases} \nabla^0 \dot{\mathbf{u}}_{m,i}^L = \mathbb{Q}_i^0 \left(\sum_j \dot{\mathbf{u}}_{m,ij} \otimes \nabla^0 W_{ij} V_j^0 \right) \tilde{\mathbb{B}}_i^{0,r} (\mathbb{Q}_i^0)^T \\ \nabla^0 \dot{\mathbf{n}}_i^L = \mathbb{Q}_i^0 \left(\sum_j \dot{\mathbf{n}}_{ij} \otimes \nabla^0 W_{ij} V_j^0 \right) \tilde{\mathbb{B}}_i^{0,n} (\mathbb{Q}_i^0)^T \end{cases} \quad (61)$$

are obtained following the consistency condition Eq. (49) and the strong-form correction Eq. (51).

3.5. Hourglass control

Inspired from Refs. [37, 30] in full-dimensional SPH for total Lagrangian solid dynamics, we introduce a hourglass control algorithm here to alleviate the hourglass modes in the dynamics of plate and shell structures.

First, we estimate the position of the inter-particle middle point linearly using the deformation gradient tensor from particles i and j , respectively, as

$$\mathbf{r}_{i+\frac{1}{2}} = \mathbf{r}_{m,i} - \frac{1}{2} \mathbb{F}_{m,i} \mathbf{r}_{m,ij}^0, \quad \mathbf{r}_{j-\frac{1}{2}} = \mathbf{r}_{m,j} + \frac{1}{2} \mathbb{F}_{m,j} \mathbf{r}_{m,ij}^0. \quad (62)$$

One can find that the inconsistency beyond linear estimation $\hat{\mathbf{r}}_{ij} = \mathbf{r}_{i+\frac{1}{2}} - \mathbf{r}_{j-\frac{1}{2}}$ is

$$\hat{\mathbf{r}}_{ij} = \mathbf{r}_{m,ij} - \frac{1}{2} (\mathbb{F}_{m,i} + \mathbb{F}_{m,j}) \mathbf{r}_{m,ij}^0. \quad (63)$$

To suppress the position inconsistency $\hat{\mathbf{r}}_{ij}$, we introduce an extra correction term to the discrete momentum conservation Eq. (55) as

$$d\rho_i^0 \ddot{\mathbf{u}}_{m,i}^{cor} = \sum_j \alpha G \beta_{ij} \gamma_{ij}^{\mathbf{r}} D \hat{\mathbf{r}}_{ij} \frac{\partial W(\mathbf{r}_{ij}^0, h)}{\partial r_{ij}^0} V_j^0 \quad (64)$$

where $\beta_{ij} = W_{ij}^0/W_0$ leads to less correction to further neighbors, $\gamma_{ij}^{\mathbf{r}} = \min(2|\hat{\mathbf{r}}_{ij}|/|\mathbf{r}_{m,ij}|, 1)$ is an adaptive limiter for less correction on the domain where the inconsistency is less pronounced, D the dimension, and parameter $\alpha = 0.002$ according to the numerical experiment and remains constant throughout this work. Note that, since the inconsistency decreases with decreasing particle spacing, different from Refs. [30], the present correction is purely numerical and vanishes with increasing resolution. Similarly, for the predicted pseudo normal, the difference of the intermediate point can be described as

$$\hat{\mathbf{n}}_{ij} = \mathbf{n}_{ij} - \mathbf{n}_{ij}^0 - \frac{1}{2} (\mathbb{F}_{\mathbf{n},i} + \mathbb{F}_{\mathbf{n},j}) \mathbf{r}_{ij}^0. \quad (65)$$

Similar with Eq. (64), the extra correction term added to the discrete angular momentum conservation Eq. (56) is

$$\frac{d^3}{12} \rho_i^0 \ddot{\mathbf{n}}_i^{cor} = \sum_j \alpha G d^2 \beta_{ij} \gamma_{ij}^{\mathbf{n}} D \hat{\mathbf{n}}_{ij} \frac{\partial W(\mathbf{r}_{ij}^0, h)}{\partial r_{ij}^0} V_j^0, \quad (66)$$

where the adaptive limiter is $\gamma_{ij}^{\mathbf{n}} = \min(2|\hat{\mathbf{n}}_{ij}|/|\mathbf{n}_{ij} - \mathbf{n}_{ij}^0|, 1)$. Note that, different with Refs. [37, 30], the present correction force is introduced in particle pairwise pattern, implying momentum conservation [7]. Also note that,

the correction force is scaled to the shear, rather than Young's, modulus, due to the fact that the hourglass modes are characterized by shear deformation [31].

3.6. Conversion between rotations and pseudo normal

Different from the mid-surface displacement, which can be numerically integrated directly from its evolution equation, the pseudo normal is not suitable for direct numerical integration since its unit magnitude may not be maintained strictly. Under the assumption of small rotation, one may have the simplified relation between the pseudo normal and rotations, i.e. $\ddot{\boldsymbol{\theta}} = (-\ddot{n}_2, \ddot{n}_1)$, so that one can obtain the rotation increment, and update rotation matrix \mathbb{R} using Rodrigues formula [46, 34] and finally the integrated pseudo normal by $\mathbf{n} = \mathbb{R}\mathbf{n}^0$.

In the present work, the numerical integration of pseudo normal is carried out without the assumption of small rotation, that is, we strictly identify the rotations and pseudo normal by using the original evolution equation and obtain their conversion relations $\ddot{\boldsymbol{\theta}} = \ddot{\boldsymbol{\theta}}(\ddot{\mathbf{n}}, \dot{\boldsymbol{\theta}}, \boldsymbol{\theta})$. Different from using the rotation matrix \mathbb{R} based on Rodrigues formula, we update the pseudo normal \mathbf{n}^L with [46, 40]

$$\mathbf{n}^L = \mathbb{R}_\eta^L \mathbb{R}_\xi^L \mathbf{n}^{0,L}, \quad (67)$$

where $\mathbb{R}_\xi^L \equiv \mathbb{R}_\xi(\theta^L)$ and $\mathbb{R}_\eta^L \equiv \mathbb{R}_\eta(\varphi^L)$ are the local rotation matrices respected to the axes ξ and η , respectively, or, equivalently, with the change rate

$$\dot{\mathbf{n}}^L = \dot{\mathbb{R}}_\eta^L \dot{\mathbb{R}}_\xi^L, \quad (68)$$

where $\dot{\mathbb{R}}_\xi^L \equiv \mathbb{R}_\xi(\theta^L, \dot{\theta}^L)$ and $\dot{\mathbb{R}}_\eta^L \equiv \mathbb{R}_\eta(\varphi^L, \dot{\varphi}^L)$. Here, the rotations and their

change rates are numerically integrated directly with the help of conversion relations.

Specifically, for a 2D problem, \mathbb{R}_ξ^L is a unit matrix, and \mathbb{R}_η^L can be described as

$$\mathbb{R}_\eta^L = \begin{bmatrix} \cos \varphi^L & \sin \varphi^L \\ -\sin \varphi^L & \cos \varphi^L \end{bmatrix}. \quad (69)$$

Then, one has the relation as

$$\mathbf{n}^L = (\sin \varphi^L, \cos \varphi^L)^T, \quad (70)$$

its 1st-order time derivative corresponding Eq. (68)

$$\dot{\mathbf{n}}^L = (\cos \varphi^L \cdot \dot{\varphi}^L, -\sin \varphi^L \cdot \dot{\varphi}^L)^T, \quad (71)$$

and 2nd-order derivative

$$\ddot{\mathbf{n}}^L = (-\sin \varphi^L \cdot (\dot{\varphi}^L)^2 + \cos \varphi^L \cdot \ddot{\varphi}^L, -\cos \varphi^L \cdot (\dot{\varphi}^L)^2 - \sin \varphi^L \cdot \ddot{\varphi}^L)^T. \quad (72)$$

Note that Eq. (72) suggests two theoretically equivalent conversion relations

$$\ddot{\varphi}^L = \frac{\ddot{n}_1^L + \sin \varphi^L \cdot (\dot{\varphi}^L)^2}{\cos \varphi^L} \quad \text{and} \quad \ddot{\varphi}^L = \frac{\ddot{n}_2^L + \cos \varphi^L \cdot (\dot{\varphi}^L)^2}{-\sin \varphi^L}. \quad (73)$$

Although each of them can be used to obtain the rotation angle φ^L and its change rate with direct numerical integration and hence the pseudo normal with Eq. (67), there are singularities at large rotation angles $\varphi^L = 0.5\pi + k\pi$ (1st relation) or $\varphi^L = k\pi$ (2nd relation) with $k = 0, 1, 2, 3, \dots$ [47, 46, 48]. In order to eliminate the singularities, we propose to use both relations with a weighted average as

$$\begin{aligned} \ddot{\varphi}^L &= (\cos \varphi^L)^2 \frac{\ddot{n}_1^L + \sin \varphi^L \cdot (\dot{\varphi}^L)^2}{\cos \varphi^L} + (\sin \varphi^L)^2 \frac{\ddot{n}_2^L + \cos \varphi^L \cdot (\dot{\varphi}^L)^2}{-\sin \varphi^L} \\ &= \cos \varphi^L \left(\ddot{n}_1^L + \sin \varphi^L \cdot (\dot{\varphi}^L)^2 \right) - \sin \varphi^L \left(\ddot{n}_2^L + \cos \varphi^L \cdot (\dot{\varphi}^L)^2 \right), \end{aligned} \quad (74)$$

which cancels both denominators. Note that the present formulation recovers $\ddot{\varphi}^L = \ddot{n}_1^L$ under the assumption of small rotation.

As for 3D problems, the rotation matrices \mathbb{R}_ξ^L and \mathbb{R}_η^L are

$$\mathbb{R}_\xi^L = \begin{bmatrix} 1 & 0 & 0 \\ 0 & \cos \theta^L & -\sin \theta^L \\ 0 & \sin \theta^L & \cos \theta^L \end{bmatrix}, \quad (75)$$

and

$$\mathbb{R}_\eta^L = \begin{bmatrix} \cos \varphi^L & 0 & \sin \varphi^L \\ 0 & 1 & 0 \\ -\sin \varphi^L & 0 & \cos \varphi^L \end{bmatrix}. \quad (76)$$

Similarly, one has the relation between rotations and pseudo normal [49]

$$\mathbf{n}^L = (\cos \theta^L \sin \varphi^L, -\sin \theta^L, \cos \theta^L \cos \varphi^L)^T, \quad (77)$$

its 1st-order time derivatives corresponding Eq. (68)

$$\begin{cases} \dot{n}_1^L = -\sin \theta^L \sin \varphi^L \dot{\theta}^L + \cos \theta^L \cos \varphi^L \dot{\varphi}^L \\ \dot{n}_2^L = -\cos \theta^L \dot{\theta}^L \\ \dot{n}_3^L = -\sin \theta^L \cos \varphi^L \dot{\theta}^L - \cos \theta^L \sin \varphi^L \dot{\varphi}^L, \end{cases} \quad (78)$$

and 2nd-order derivatives

$$\begin{cases} \ddot{n}_1^L = -\sin \theta^L \sin \varphi^L \ddot{\theta}^L - \cos \theta^L \sin \varphi^L (\dot{\theta}^L)^2 - 2 \sin \theta^L \cos \varphi^L \dot{\theta}^L \dot{\varphi}^L \\ \quad - \cos \theta^L \sin \varphi^L (\dot{\varphi}^L)^2 + \cos \theta^L \cos \varphi^L \ddot{\varphi}^L \\ \ddot{n}_2^L = \sin \theta^L (\dot{\theta}^L)^2 - \cos \theta^L \ddot{\theta}^L \\ \ddot{n}_3^L = -\sin \theta^L \cos \varphi^L \ddot{\theta}^L - \cos \theta^L \cos \varphi^L (\dot{\theta}^L)^2 + 2 \sin \theta^L \cos \varphi^L \dot{\theta}^L \dot{\varphi}^L \\ \quad - \cos \theta^L \cos \varphi^L (\dot{\varphi}^L)^2 - \cos \theta^L \sin \varphi^L \ddot{\varphi}^L. \end{cases} \quad (79)$$

Note that, one can obtained 3 theoretically equivalent conversion relations, respectively, by 1st and 3rd expressions of Eq. (79) as

$$\begin{cases} \ddot{\theta}^L = - \left(\ddot{n}_3^L \cos \varphi^L + \ddot{n}_1^L \sin \varphi^L + (\dot{\varphi}^L)^2 \cos \theta^L + (\dot{\theta}^L)^2 \cos \theta^L \right) / \sin \theta^L \\ \ddot{\varphi}^L = \left(\ddot{n}_1^L \cos \varphi^L - \ddot{n}_3^L \sin \varphi^L + 2\dot{\varphi}^L \dot{\theta}^L \sin \theta^L \right) / \cos \theta^L, \end{cases} \quad (80)$$

1st and 2nd expressions

$$\begin{cases} \ddot{\theta}^L = \left(\sin \theta^L (\dot{\theta}^L)^2 - \ddot{n}_2^L \right) / \cos \theta^L \\ \ddot{\varphi}^L = \left(\ddot{n}_1^L \cos \theta^L + (\dot{\varphi}^L)^2 \cos^2 \theta^L \sin \varphi^L + (\dot{\theta}^L)^2 \sin \varphi^L - \ddot{n}_2^L \sin \varphi^L \sin \theta^L \right. \\ \quad \left. + 2\dot{\varphi}^L \dot{\theta}^L \cos \varphi^L \cos \theta^L \sin \theta^L \right) / \cos \varphi^L \cos^2 \theta^L, \end{cases} \quad (81)$$

and 2nd and 3rd expressions

$$\begin{cases} \ddot{\theta}^L = \left(\sin \theta^L (\dot{\theta}^L)^2 - \ddot{n}_2^L \right) / \cos \theta^L \\ \ddot{\varphi}^L = - \left(\ddot{n}_3^L \cos \theta^L + (\dot{\varphi}^L)^2 \cos \varphi^L \cos^2 \theta^L + (\dot{\theta}^L)^2 \cos \varphi^L - \ddot{n}_2^L \cos \varphi^L \sin \theta^L \right. \\ \quad \left. - 2\dot{\varphi}^L \dot{\theta}^L \cos \theta^L \sin \varphi^L \sin \theta^L \right) / \sin \varphi^L \cos^2 \theta^L. \end{cases} \quad (82)$$

Again, each of these conversion relations suffers singularities at large rotations similar to that of 2D formulations. To eliminate the singularities, we first apply the weighted average to the conversion between between $\ddot{\theta}^L$ and \ddot{n}^L with Eqs. (80) and (81) as

$$\begin{aligned} \ddot{\theta}^L = & - \left(\ddot{n}_3^L \cos \varphi^L + \ddot{n}_1^L \sin \varphi^L + (\dot{\varphi}^L)^2 \cos \theta^L + (\dot{\theta}^L)^2 \cos \theta^L \right) \sin \theta^L \\ & + \left(\sin \theta^L (\dot{\theta}^L)^2 - \ddot{n}_2^L \right) \cos \theta^L. \end{aligned} \quad (83)$$

Then, for the conversion relation between $\ddot{\varphi}^L$ and \ddot{n}^L , according to Eq. (80),

we can rewrite the relation as

$$\cos \theta^L = B/\ddot{\varphi}^L, \quad (84)$$

where B denotes the numerator of the 2nd expression in Eq. (80). We further denote the numerators of the 2nd expressions in Eqs. (81) and (82), respectively, as B_1 and B_2 . Inserting Eq. (84) into Eqs. (81) and (82), we have

$$\begin{cases} \ddot{\varphi}^L = (B^2 \cos \varphi^L) / B_1 \\ \ddot{\varphi}^L = (B^2 \sin \varphi^L) / B_2, \end{cases} \quad (85)$$

and obtain the weighted average of the conversion relation as

$$\ddot{\varphi}^L = \frac{B_1 B^2 \cos \varphi^L + B_2 B^2 \sin \varphi^L}{B_1^2 + B_2^2}. \quad (86)$$

Again, one can easily find that the present relations recover $\ddot{\boldsymbol{\theta}}^L = (\ddot{\theta}^L, \ddot{\varphi}^L) = (-\ddot{n}_2^L, \ddot{n}_1^L)$ for small rotations.

3.7. Time stepping

For the time integration of plate and shell dynamics, we use the position-based Verlet scheme [50]. At the beginning of each time step, the deformation gradient, particle position, rotation angles and pseudo normal are updated to the midpoint of the n -th time step as

$$\begin{cases} \mathbb{F}^{L,n+\frac{1}{2}} = \mathbb{F}^{L,n} + \frac{1}{2}\Delta t \dot{\mathbb{F}}^{L,n} \\ \mathbf{r}_m^{n+\frac{1}{2}} = \mathbf{r}_m^n + \frac{1}{2}\Delta t \dot{\mathbf{r}}_m^n \\ \boldsymbol{\theta}^{L,n+\frac{1}{2}} = \boldsymbol{\theta}^{L,n} + \frac{1}{2}\Delta t \dot{\boldsymbol{\theta}}^{L,n} \\ \mathbf{n}^{L,n+\frac{1}{2}} = \mathbf{n}^{L,n} + \frac{1}{2}\Delta t \dot{\mathbf{n}}^{L,n}. \end{cases} \quad (87)$$

After the stress correction and Gauss-Legendre quadrature Eqs. (21) and (23), the conservation equations are solved to obtain the $\dot{\mathbf{u}}_m^{n+1}$ and $\dot{\mathbf{n}}^{n+1}$. After transforming $\dot{\mathbf{n}}^{n+1}$ to $\dot{\mathbf{n}}^{L,n+1}$, $\dot{\boldsymbol{\theta}}^{L,n+1}$ is obtained through the conversion relation between the pseudo normal and rotation angle, i.e., Eq. (74) for 2D problems and Eqs. (83) and (86) for 3D problems. At this point, the velocity and angular velocity are updated by

$$\begin{cases} \dot{\mathbf{u}}_m^{n+1} = \dot{\mathbf{u}}_m^n + \Delta t \ddot{\mathbf{u}}_m^{n+1} \\ \dot{\boldsymbol{\theta}}^{L,n+1} = \dot{\boldsymbol{\theta}}^{L,n} + \Delta t \ddot{\boldsymbol{\theta}}^{L,n+1}, \end{cases} \quad (88)$$

and the change rate of pseudo normal $\dot{\mathbf{n}}$ is updated by Eq. (71) or (78). Finally, the change rate of the deformation gradient $\dot{\mathbb{F}}^{L,n+1}$ is estimated by Eq. (60), and then the deformation gradient, density, particle position, rotation angles and pseudo normal are updated to the new time step with

$$\begin{cases} \mathbb{F}^{L,n+1} = \mathbb{F}^{L,n+\frac{1}{2}} + \frac{1}{2} \Delta t \dot{\mathbb{F}}^{L,n+1} \\ \rho^{n+1} = (J_m^{n+1})^{-1} \rho^0 \\ \mathbf{r}_m^{n+1} = \mathbf{r}_m^{n+\frac{1}{2}} + \frac{1}{2} \Delta t \dot{\mathbf{u}}_m^{n+1} \\ \boldsymbol{\theta}^{L,n+1} = \boldsymbol{\theta}^{L,n+\frac{1}{2}} + \frac{1}{2} \Delta t \dot{\boldsymbol{\theta}}^{L,n+1} \\ \mathbf{n}^{L,n+1} = \mathbf{n}^{L,n+\frac{1}{2}} + \frac{1}{2} \Delta t \dot{\mathbf{n}}^{L,n+1}. \end{cases} \quad (89)$$

For the numerical stability, the time-step size Δt is given by

$$\Delta t = \text{CFL} \min(\Delta t_1, \Delta t_2, \Delta t_3), \quad (90)$$

where

$$\begin{cases} \Delta t_1 = \min \left(\frac{h}{c_v + |\dot{\mathbf{u}}_m|_{max}}, \sqrt{\frac{h}{|\ddot{\mathbf{u}}_m|_{max}}} \right) \\ \Delta t_2 = \min \left(\frac{1}{c_v + |\dot{\boldsymbol{\theta}}^L|_{max}}, \sqrt{\frac{1}{|\ddot{\boldsymbol{\theta}}^L|_{max}}} \right) \\ \Delta t_3 = h \left(\frac{\rho(1-\nu^2)/E}{2+(\pi^2/12)(1-\nu)[1+1.5(h/d)^2]} \right)^{1/2}. \end{cases} \quad (91)$$

Note that the time-step size Δt_3 follows the Refs. [34, 51] and depends on the thickness and material properties, and the present Courant-Friedrichs-Lewy (CFL) number is set as 0.6. An overview of the complete solution procedure is presented in Algorithm 1.

Algorithm 1: The present SPH method for plate/shell structures.

- 1 Setup parameters and initialize the simulation;
 - 2 Construct the particle-neighbor list and compute the kernel values;
 - 3 Compute the correction matrices $\tilde{\mathbb{B}}^{0,r}$ and $\tilde{\mathbb{B}}^{0,n}$ for each particle (Section 3.2);
 - 4 **while** *simulation is not finished* **do**
 - 5 Compute the time-step size Δt using Eq. (90);
 - 6 Update the deformation gradient tensor \mathbb{F}^L , particle position \mathbf{r}_m , rotation angle $\boldsymbol{\theta}^L$ and pseudo normal \mathbf{n} for half time step $\Delta t/2$;
 - 7 Compute and correct the Cauchy stress $\boldsymbol{\sigma}^l$ (Sections 2.1.2 and 2.1.3);
 - 8 Compute the resultants \mathbb{N}^l and \mathbb{M}^l , and shear force \mathbf{Q}^l (Eq. (26));
 - 9 Compute the acceleration $\ddot{\mathbf{u}}_m$ (Eqs. (55) and (64)) and $\ddot{\mathbf{n}}$ (Eqs. (56) and (66));
 - 10 Compute the angular acceleration $\ddot{\boldsymbol{\theta}}^L$ (Eq. (74) for 2D problems, and Eqs. (83) and (86) for 3D problems);
 - 11 Update the velocity $\dot{\mathbf{u}}_m$ and angular velocity $\dot{\boldsymbol{\theta}}^L$ for a time step Δt ;
 - 12 Compute the change rate of pseudo normal $\dot{\mathbf{n}}^L$ using Eq. (71) or (78);
 - 13 Compute the change rate of the deformation gradient tensor $\partial\mathbb{F}^L/\partial t$ (Eq. (60));
 - 14 Update the deformation gradient tensor \mathbb{F}^L , density ρ , particle position \mathbf{r}_m , rotation angle $\boldsymbol{\theta}^L$ and pseudo normal \mathbf{n} for another half time step $\Delta t/2$;
 - 15 **end**
 - 16 Terminate the simulation.
-

4. Numerical examples

To demonstrate the accuracy and stability of the proposed surface-particle SPH method (denoted as shell method), this section investigates a series of benchmark tests where analytical or numerical reference data from the literature or/and volume-particle SPH method (denoted as volume method) are available for qualitative and quantitative comparison. The smoothing length $h = 1.15 dp$, where dp denotes the initial particle spacing, is employed in all the following simulations.

4.1. 2D oscillating plate strip

The first example involves a plate strip with initial uniform transverse velocity along the length with one edge fixed and the others free, which has previously been theoretically [52] and numerically [53, 54, 31] investigated in the literature. As shown in Figure 3(a), this plate strip is assumed to be infinitely long along the y -axis with a finite width $a = 0.2$ m along the x -axis. To demonstrate that both thin and moderately thick structures can be simulated, this plate strip is modeled with the thicknesses $d = 0.01$ m and 0.001 m. The material properties are set as follows: density $\rho_0 = 1000.0$ kg/m³, Young's modulus $E = 2.0$ MPa, and Poisson's ratio ν varies for different cases. Figure 3(b) shows the discrete model of the chosen cross-section with clamped edges at $x = 0$. The transverse velocity v_z is applied to the plate strip as

$$v_z(x) = v_f c \frac{f(x)}{f(a)}, \quad (92)$$

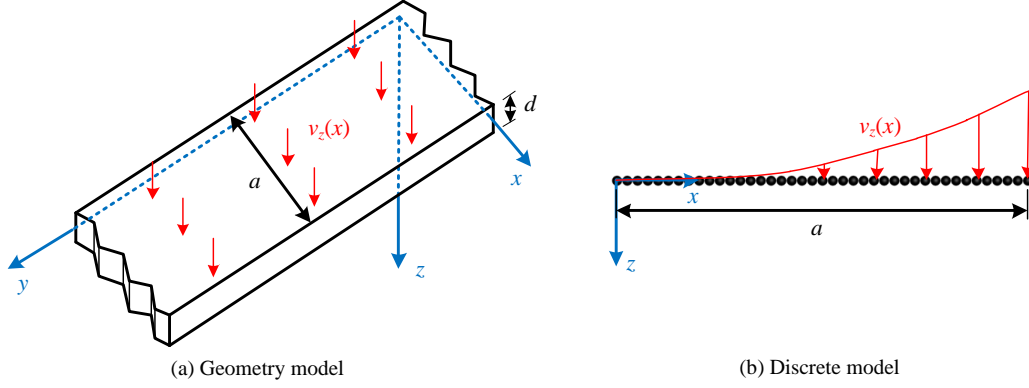


Figure 3: 2D oscillating plate strip: Initial configuration with width $a = 0.2$ m.

where v_f is a constant that varies with different cases, and

$$\begin{aligned}
 f(x) &= (\sin(ka) + \sinh(ka)) (\cos(kx) - \cosh(kx)) \\
 &\quad - (\cos(ka) + \cosh(ka)) (\sin(kx) - \sinh(kx))
 \end{aligned} \tag{93}$$

with k determined by

$$\cos(ka) \cosh(ka) = -1 \tag{94}$$

and $ka = 1.875$. The frequency ω of the oscillating plate strip is theoretically given by

$$\omega^2 = \frac{Ed^2k^4}{12\rho(1-\nu^2)}. \tag{95}$$

Figure 4 shows the particles with von Mises stress $\bar{\sigma}$ contour for the case of $d = 0.001$ m, $v_f = 0.01$, $\nu = 0.4$, and the initial particle spacing $dp = a/40 = 0.005$ m. It should be noted that the present method predicts smooth deformation and stress fields without singularities for large rotations (more than π). Three different spatial resolutions, $a/dp = 40$, $a/dp = 80$, and $a/dp = 160$, are tested in the convergence study. Figure 5 shows the time history of vertical position z of the strip endpoint with $d = 0.01$ m, $v_f =$

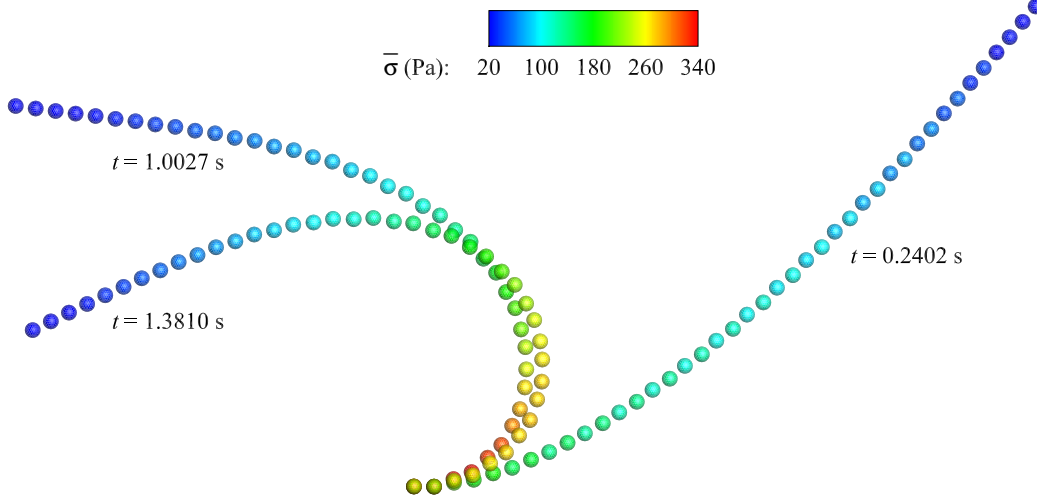


Figure 4: 2D oscillating plate strip: Deformed particle configuration colored by von Mises stress $\bar{\sigma}$ of the mid-surface at serial time instants with the width $a = 0.2$ m, thickness $d = 0.02$ m, $v_f = 0.01$, and spatial particle resolution $a/dp = 40$. The material is modeled with density $\rho_0 = 1000.0$ kg/m³, Young's modulus $E = 2.0$ MPa, and Poisson's ratio $\nu = 0.4$.

0.025 and $\nu = 0.4$. It can be observed that typical 2nd-order convergence has been achieved. In addition, a long-term simulation is performed herein to demonstrate the numerical stability of the proposed formulation. For quantitative validation, Tables 1 and 2 detail the oscillation period T for a wide range of v_f and ν , obtained by the present method with the spatial particle resolution $a/dp = 160$, when thickness $d = 0.01$ m and 0.001 m, respectively, and the comparison to theoretical solution obtained from small perturbation analysis. The differences, which are less than 8.00% for $\nu = 0.22$ and decrease to about 5.00% when the Poisson's ratio is increased to 0.4, are acceptable.

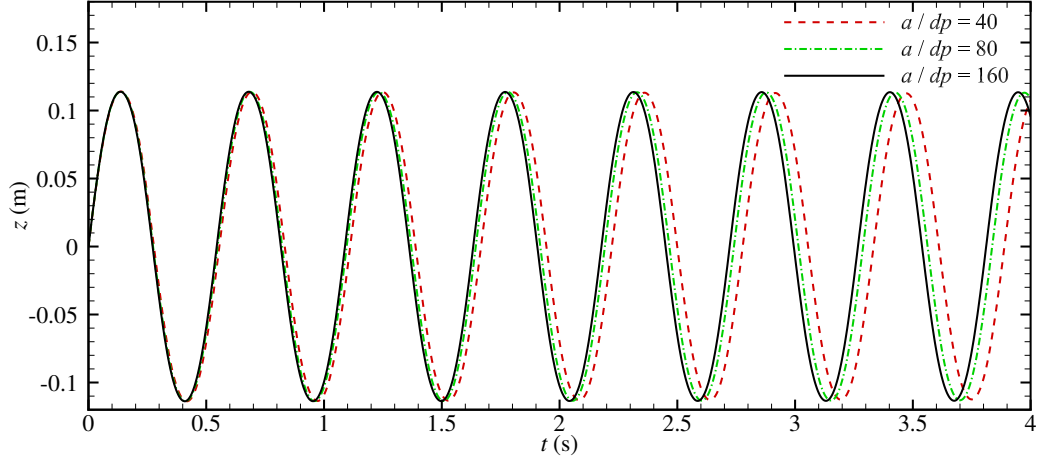


Figure 5: 2D oscillating plate strip: Time history of the vertical position z observed at the plate strip endpoint when $d = 0.01$ m, $v_f = 0.025$ and $\nu = 0.4$.

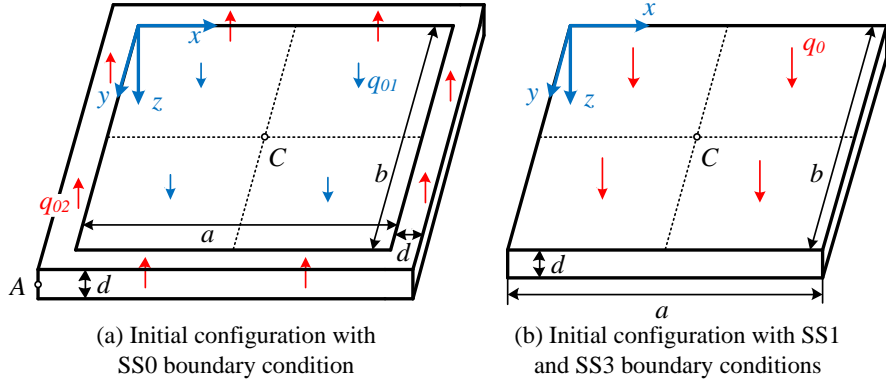


Figure 6: 3D square plate: Problem setup with $a = b = 254$ mm and thickness $d = 25.4$ mm.

4.2. 3D square plate

In this section, a 3D square plate under different types of boundary conditions is considered for quasi-steady analyses, as shown in Figure 6. With side length $a = b = 254$ mm and thickness $d = 25.4$ mm, the plate material is defined with density $\rho_0 = 1600$ kg/m³, Young's modulus $E = 53.7791$ GPa

Table 1: 2D oscillating plate strip: Quantitative validation of the oscillation period for $a = 0.2$ m and $d = 0.01$ m with various v_f and ν .

v_f	ν	$T_{\text{Shell model}}$	$T_{\text{Theoretical}}$	Error
0.025	0.22	0.58137	0.54018	7.63%
0.05	0.22	0.57715	0.54018	6.92%
0.1	0.22	0.56801	0.54018	5.15%
0.025	0.30	0.56804	0.52824	7.53%
0.05	0.30	0.56308	0.52824	6.60%
0.1	0.30	0.55481	0.52824	5.03%
0.025	0.40	0.54447	0.50752	7.28%
0.05	0.40	0.53683	0.50752	5.78%
0.1	0.40	0.53252	0.50752	4.93%

and Poisson's ratio $\nu = 0.3$. Three types of boundary conditions denoted as SS0, SS1 and SS3 following Refs. [42, 34] are implemented as

- ▶ SS0: constrained mass center without constrained boundaries;
- ▶ SS1: $u = w = \varphi = 0$ on edges parallel to x -axis and $v = w = \theta = 0$ on edges parallel to y -axis;
- ▶ SS3: $u = v = w = 0$ on all edges.

Note that, for the case of SS0, the outer square ring with width d is imposed with negative pressure q_{02} . The uniformly distributed loads are parameterized by the loading factors \bar{P} and \bar{P}_1 as $q_0 = \bar{P}E(d/a)^4$, $q_{01} = \bar{P}_1E(d/a)^4$

Table 2: 2D oscillating plate strip: Quantitative validation of the oscillation period for $a = 0.2$ m and $d = 0.001$ m with various v_f and ν .

v_f	ν	$T_{\text{Shell model}}$	$T_{\text{Theoretical}}$	Error
0.0025	0.22	5.80249	5.40182	7.42%
0.005	0.22	5.75544	5.40182	6.55%
0.01	0.22	5.64181	5.40182	4.44%
0.0025	0.30	5.66756	5.28243	7.29%
0.005	0.30	5.61006	5.28243	6.20%
0.01	0.30	5.49156	5.28243	3.96%
0.0025	0.40	5.42826	5.07519	6.96%
0.005	0.40	5.34224	5.07519	5.26%
0.01	0.40	5.27522	5.07519	3.94%

and $q_{02}(2ad + 2bd + 4d^2) = q_{01}ab$, so that the applied negative force along the z -axis prevents the center of mass from moving.

For comprehensive validation, a convergence study of tests with SS0 is conducted, and the results are compared with those obtained by the volume method released in the SPHinXsys repository [9]. Figure 7 shows the particle distribution and stress fields under the loading factor $\bar{P}_1 = 25$ with the spatial discretization $d/dp = 8$. Figure 8 shows the non-dimensional deflection $\bar{w}_C = w_C/d$ and $\bar{w}_A = w_A/d$ probed at the central point C and corner point A , respectively, obtained by both SPH shell and volume methods. It should be emphasized that there are only quite small differences between the results

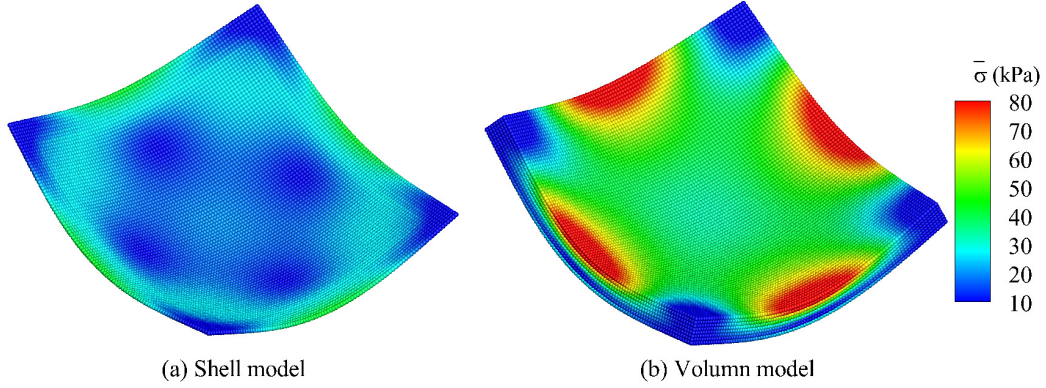


Figure 7: 3D square plate: Particles colored by von Mises stress $\bar{\sigma}$ of tests with SS0 obtained by the present shell (left) and volume (right) methods under the loading factor $\bar{P}_1 = 25$. Note that the left panel shows the stress $\bar{\sigma}$ of the plate mid-surface. The material is modeled with the density $\rho_0 = 1600 \text{ kg/m}^3$, Young's modulus $E = 53.7791 \text{ GPa}$ and Poisson's ratio $\nu = 0.3$. The spatial particle resolution is set as $d/dp = 8$.

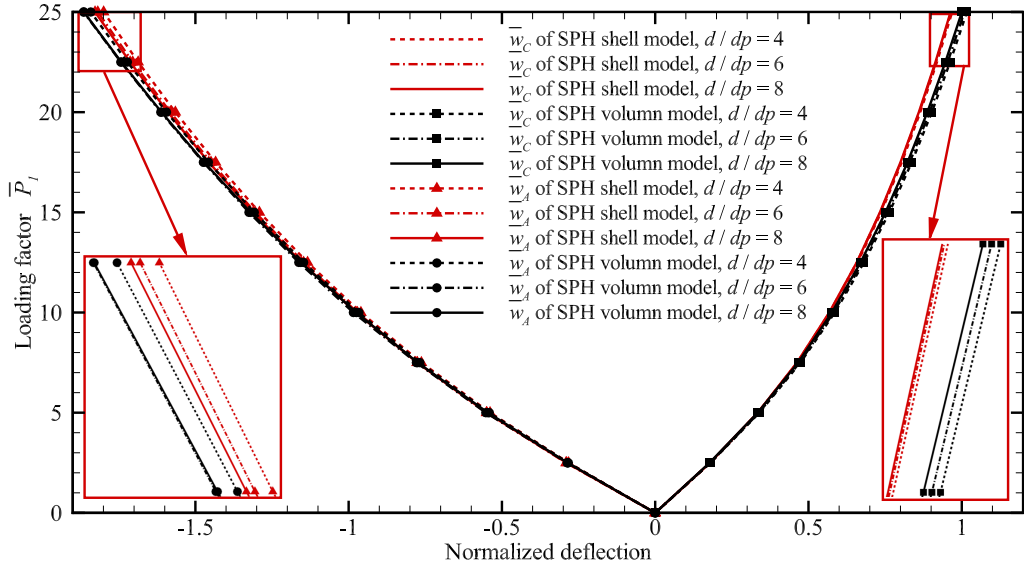


Figure 8: 3D square plate: Load-deflection curves of tests with SS0 under three different spatial resolutions, and their comparison with those of the volume method [9].

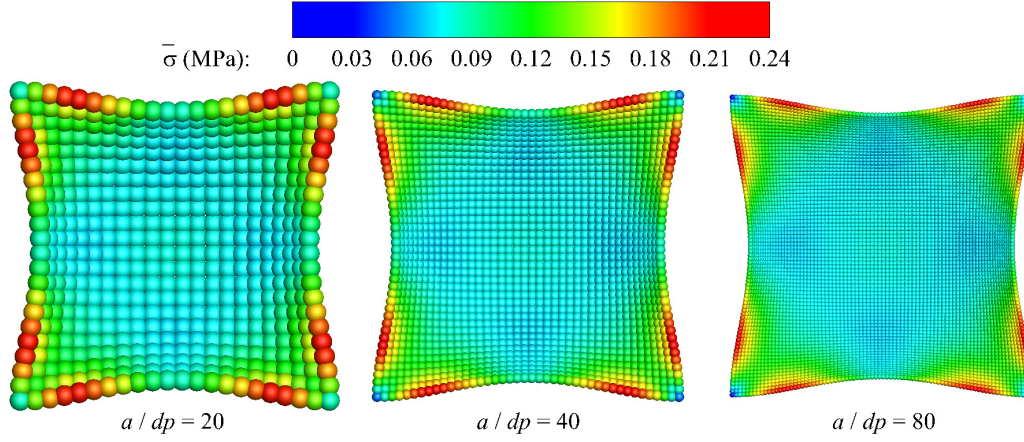
of the present reduced-dimensional and full-dimensional models.

The particles colored by von Mises stress $\bar{\sigma}$ at the mid-surface for three spatial discretizations, $a/dp = 20$, $a/dp = 40$ and $a/dp = 80$, with the SS1 and SS3 boundary conditions under $\bar{P} = 200$ are shown in Figure 9. It can be observed that the regular particle distribution and smooth stress field are obtained. Also, both the deformation and von Mises stress $\bar{\sigma}$ exhibit good convergence properties with particle refinement. In order to demonstrate the accuracy of the present method, the non-dimensional deflections \bar{w}_C for tests with SS1 and SS3 under various spatial resolutions are compared to those of the Ref. [42]. As shown in Figs. 10, the numerical results quickly converge to the reference solutions obtained by the finite element method (FEM) with increasing resolution.

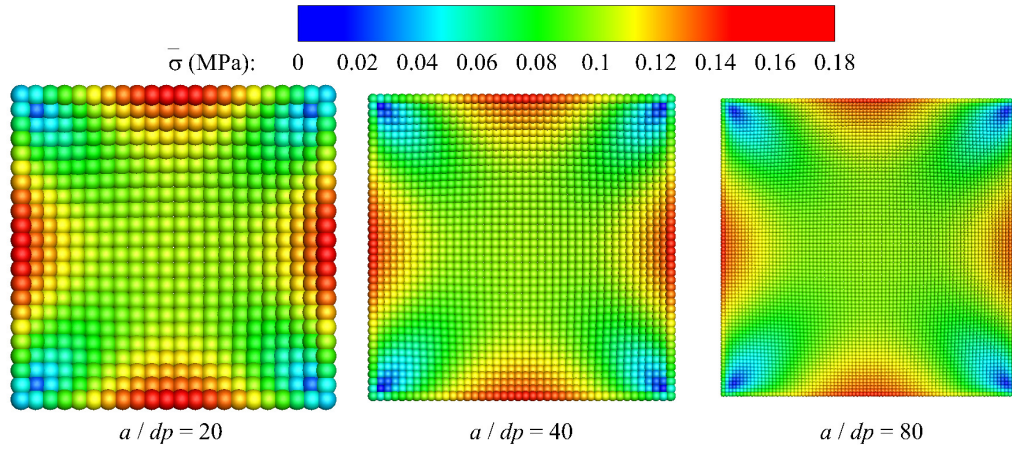
4.3. Dynamic response of a 3D square plate

Following Ref. [55], the 3D square plate studied in Section 4.2 is considered herein with the thickness $d = 12.7$ mm and Young's modulus $E = 68.94$ GPa. The SS0 and SS3 boundary conditions are applied for dynamic analyses under a step loading of uniform normal pressure $q_{01} = q_0 = 2.068427$ MPa. For convergence study, three different spatial discretizations, i.e., $d/dp = 2$, $d/dp = 4$ and $d/dp = 8$, are considered.

For quantitative validation, Figure 11 shows the time history of the deflections w_C probed at the central point C and w_A at the corner point A with SS0 boundary condition and its comparison to the results obtained by the volume method. Also, Figure 12 shows the time history of the deflection w_C with the SS3 boundary condition and its comparison with that of Ref. [55]. In general, the present results are in good agreements with those obtained



(a) SS1 boundary conditon



(b) SS3 boundary conditon

Figure 9: 3D square plate: Particles colored by von Mises stress $\bar{\sigma}$ of the mid-surface with particle refinement under the loading factor $\bar{P} = 200$ and SS1 and SS3 boundary conditions. The plate material has parameters of the density $\rho_0 = 1600 \text{ kg/m}^3$, Young's modulus $E = 53.7791 \text{ GPa}$ and Poisson's ratio $\nu = 0.3$.

by the volume method and of Ref. [55].

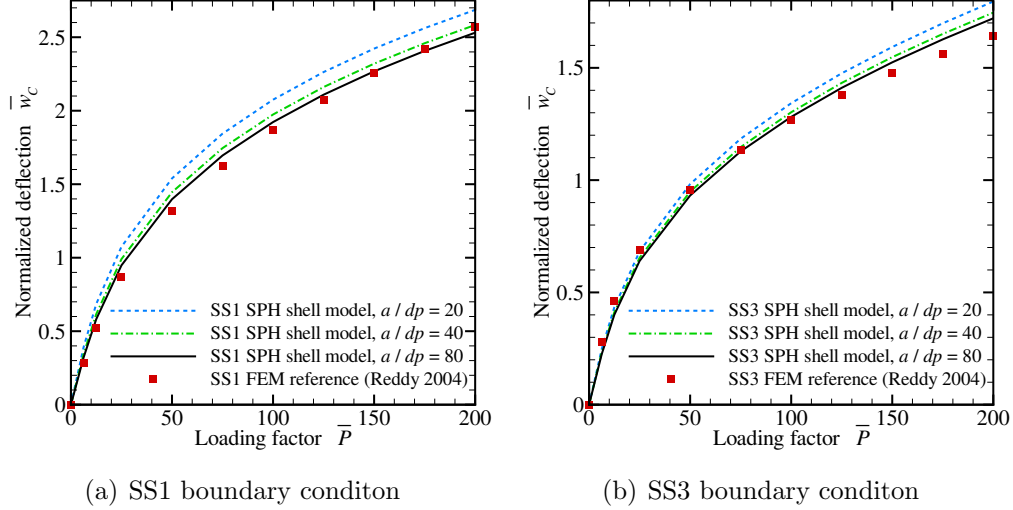


Figure 10: 3D square plate: Load-deflection curves of tests with SS1 and SS3 under three different spatial resolutions, and their comparison with that of Reddy [42].

4.4. 3D cantilevered plate

Following Refs [56, 57, 58], the static response of a 3D cantilevered plate subjected to a distributed end shear load f_0 is considered. As shown in Figure 13, the plate with length $a = 10$ m, width $b = 1$ m and thickness $d = 0.1$ m is clamped at $y = 0$, and has material parameters of density $\rho_0 = 1100$ kg/m³, Young's modulus $E = 1.2$ MPa and Poisson's ratio $\nu = 0.0$. The shear load is parameterized by a loading factor \bar{F} as $f_0 = \bar{F}EI/a^2$ with the inertia moment $I = bd^3/12$. Three different resolutions, i.e., $b/dp = 5$, $b/dp = 7$ and $b/dp = 9$, are considered for convergence study.

Figure 14 shows the particles colored by the vertical displacement under different loading factor \bar{F} at the spatial resolution $b/dp = 9$. A regular particle distribution and smooth vertical displacement field are noted. Figure 15 gives the displacement u_c and w_c of the point C , defined in Figure 13, as a

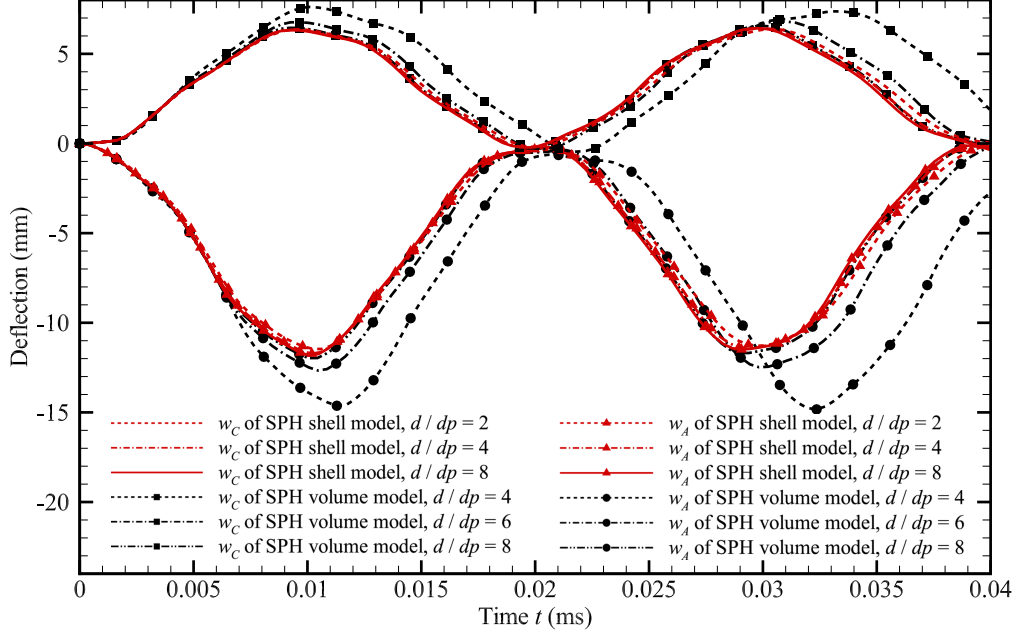


Figure 11: 3D square plate with dynamic response: Time history of the deflection w_C and w_A probed at the central point C and corner point A , respectively, with SS0 boundary condition. The material is modeled with the density $\rho_0 = 1600 \text{ kg/m}^3$, Young's modulus $E = 68.94 \text{ GPa}$ and Poisson's ratio $\nu = 0.3$.

function of the loading factor \bar{F} and the initial particle spacing dp , and their comparison with those in Ref. [58]. It can be noted that the displacement is converging rapidly, again at about 2nd-order, with increasing resolution, demonstrating the accuracy of the present method.

4.5. Scordelis-Lo roof

As shown in Figure 16, the Scordelis-Lo roof with length $a = 50 \text{ m}$, radius $r = 25 \text{ m}$, thickness $d = 0.25 \text{ m}$ and $\beta = 40^\circ$ is considered herein, and the material properties are density $\rho_0 = 36 \text{ kg/m}^3$, Young's modulus $E = 432 \text{ MPa}$ and zero Poisson's ratio. The roof is supported at its ends by

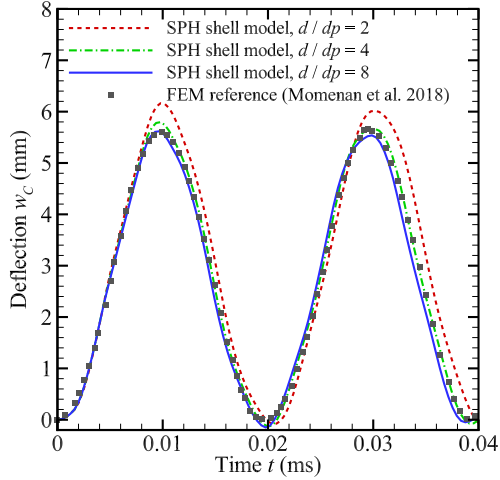


Figure 12: 3D square plate with dynamic response: Time history of the deflection w_C observed at the central point C with SS3 boundary condition.

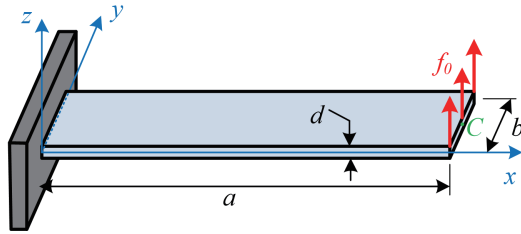


Figure 13: 3D cantilevered plate: Initial configuration with the length $a = 10$ m, width $b = 1$ m and thickness $d = 0.1$ m.

fixed diaphragms, i.e. the translations in x and z directions are constrained, and subjected to a gravity loading of $g = 10$ m/s².

The FEM solution of the vertical displacement w at the midpoint of the side edge converges to 0.3024 m as reported in Refs. [59, 60]. A sequentially refined resolutions of $b/dp = 15, 20, 25, 30$ and 40 with $b = 2r\beta$ denoting the arc length of the roof end are considered to assess the convergence property

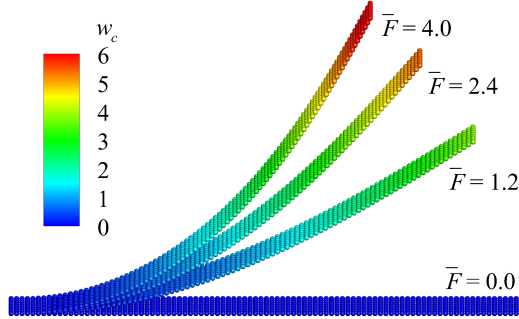


Figure 14: 3D cantilevered plate: Particles colored by the vertical displacement w_c under the various loading factor \bar{F} at spatial resolution $b/dp = 9$. The material is set as the density $\rho_0 = 1100 \text{ kg/m}^3$, Young's modulus $E = 1.2 \text{ MPa}$ and Poisson's ratio $\nu = 0.0$.

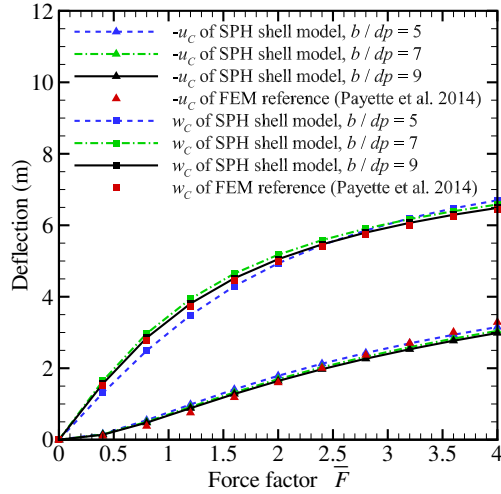


Figure 15: 3D cantilevered plate: Load-deflection curves with three various spatial discretizations, and their comparison with that of Payette et al. [58].

of the present method. Figure 17 shows the particles colored with the von Mises stress $\bar{\sigma}$ of the mid-surface obtained at different resolutions. The regular particle distribution and smooth stress fields are noted. With increasing resolution, a clear convergence is exhibited. The profile of displacement w

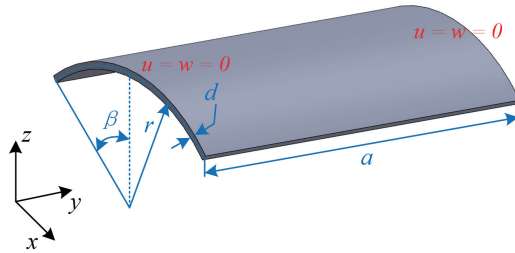


Figure 16: Scordelis-Lo roof: Initial configuration with the length $a = 50$ m, radius $r = 25$ m, thickness $d = 0.25$ m and $\beta = 40^\circ$.

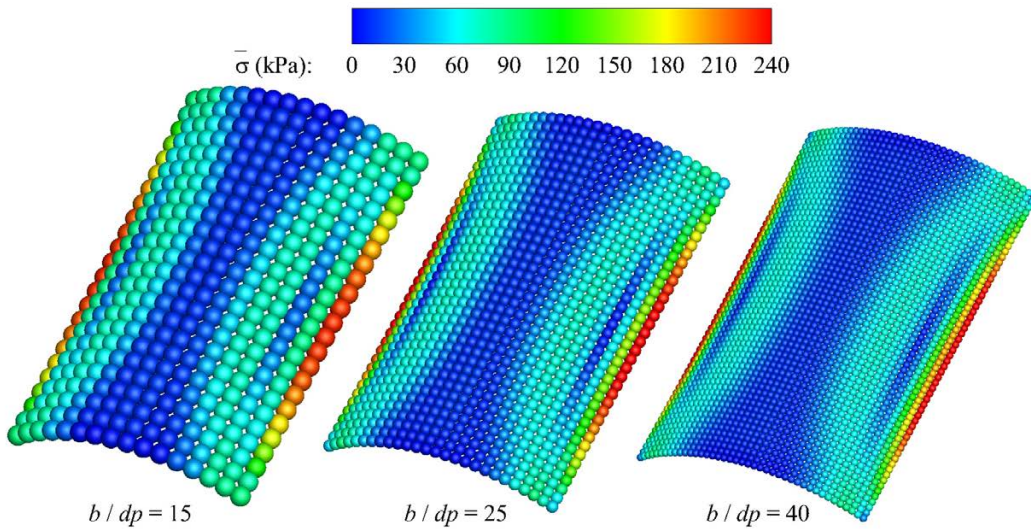


Figure 17: Scordelis-Lo roof: Particles colored by the von Mises stress $\bar{\sigma}$ of the mid-surface obtained by the present method with particle refinement. The material is set as the density $\rho_0 = 36$ kg/m³, Young's modulus $E = 432$ MPa and Poisson's ratio $\nu = 0.0$.

with varying spatial resolution obtained by the present method is depicted in Figure 18. It can be noted that the result converges rapidly to $w = 0.2991$ m when $b/dp = 40$ with 1.09% error compared to the solution of Refs. [59, 60].

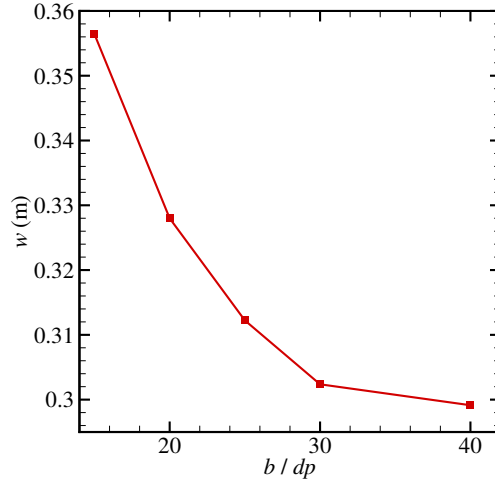


Figure 18: Scordelis-Lo roof: Convergence study of the displacement obtained by the present method with particle refinement.

4.6. Pinched hemispherical shell

We now consider a pinched hemispherical shell with an 18° circular cutout at its pole following Refs. [61, 62, 63, 57, 58]. As shown in Figure 19(a), the hemispherical shell with the radius $r = 10.0$ m and thickness $d = 0.04$ m is loaded by four alternating radial point forces \mathbf{F} , prescribed along the equator at 90° intervals. A linear elastic material with the density $\rho_0 = 1100$ kg/m³, Young's modulus $E = 68.25$ MPa and Poisson's ratio $\nu = 0.3$ is applied.

Figure 19(b-d) shows the distribution of von Mises stress $\bar{\sigma}$ at the mid-surface under varying magnitude of the point force \mathbf{F} . The regular particle distribution is observed, although slight stress fluctuation is exhibited near the place where the point force is applied. For quantitative analysis and convergence study, the radial deflections w_A and w_B of monitoring points A and B as a function of the point force magnitude and resolution are compared

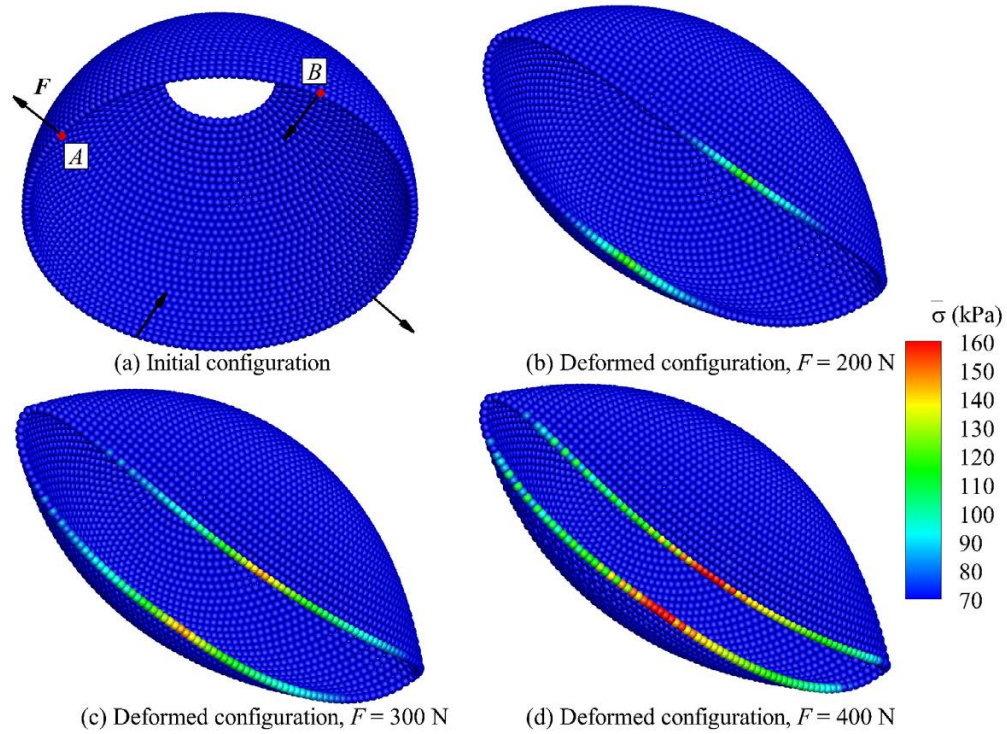


Figure 19: Pinched hemispherical shell: (a) Initial configuration with the radius of the mid-surface $r = 10.0$ m and thickness $d = 0.04$ m, (b-d) particles colored by the von Mises stress $\bar{\sigma}$ of the mid-surface under 3 point force magnitudes at spatial discretization $2\pi r/dp = 160$. The material parameters are set as the density $\rho_0 = 1100$ kg/m³, Young's modulus $E = 68.25$ MPa and Poisson's ratio $\nu = 0.3$.

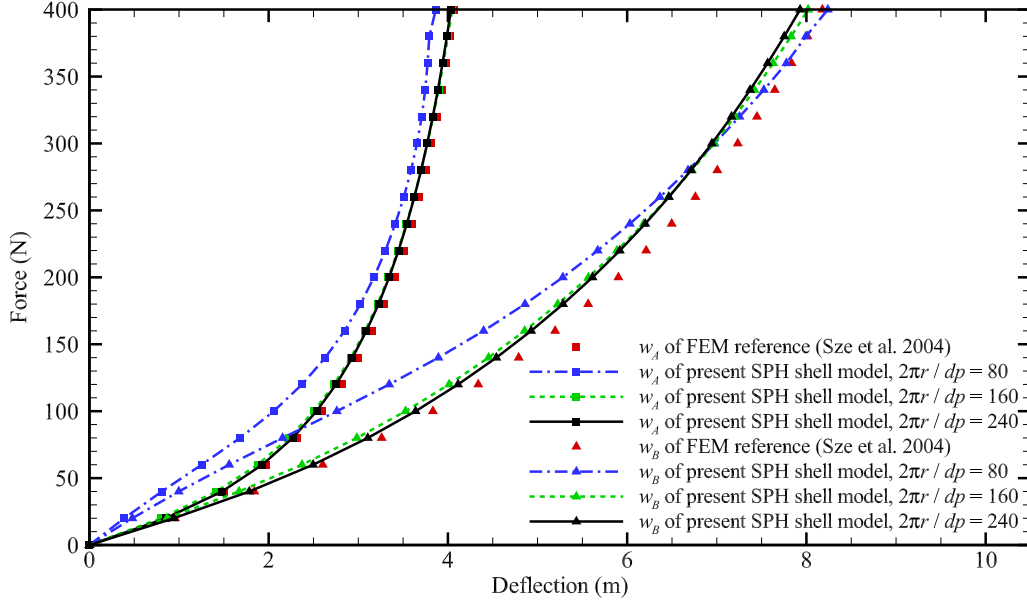


Figure 20: Pinched hemispherical shell: Curves of radical displacements of points A and B as a function of the point force magnitude and spatial resolution, and their comparison with those of Sze et al. [57].

with those of Ref. [57]. Three different spatial discretizations, i.e., $2\pi r/dp = 80, 160$ and 240 , are considered for convergence study. As shown in Figure 20, the results of present SPH shell model is quickly converging to those of Ref. [57].

4.7. Pulled-out cylindrical shell

A more challenging benchmark test with large displacements is considered in this section following Refs. [29, 64]. As shown in Figure 21, a cylindrical shell with the radius $r = 5.0$ m, length $a = 10.35$ m and thickness $d = 0.094$ m is subjected to a pair of point forces \mathbf{F} which are equal in magnitude and opposite in direction. A linear elastic material with the density $\rho_0 =$

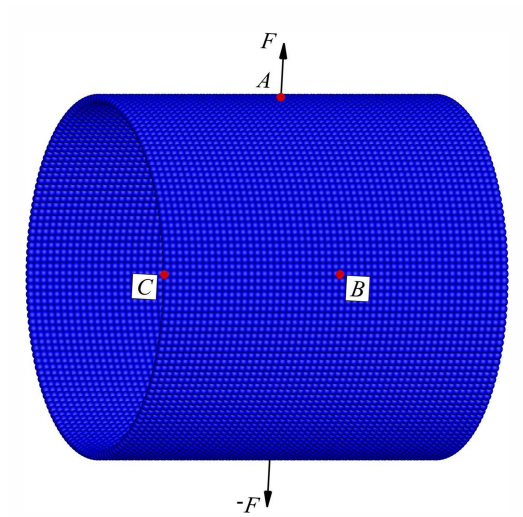


Figure 21: Pulled-out cylindrical shell: Initial configuration with the radius of the mid-surface $r = 5.0$ m, length $a = 10.35$ m and thickness $d = 0.094$ m.

1100 kg/m^3 , Young's modulus $E = 10.5 \text{ MPa}$ and Poisson's ratio $\nu = 0.3125$ is applied.

Figure 22 shows the distribution of von Mises stress $\bar{\sigma}$ at the mid-surface under varying magnitude of the point force \mathbf{F} . The regular particle distribution and smooth stress fields, even close to the place where the point force is applied, are observed. For quantitative analysis and convergence study, the radial displacements w_A , w_B and w_C of monitoring points A , B and C as a function of the point force magnitude and resolution are compared with those of Ref. [29, 64]. Three different spatial discretizations, i.e., $b/dp = 80, 160$ and 240 with $b = 2\pi r$ denoting the circumference length of the end, are considered for convergence study. As shown in Figure 23, the bifurcation point of the curve is accurately predicted, suggesting good

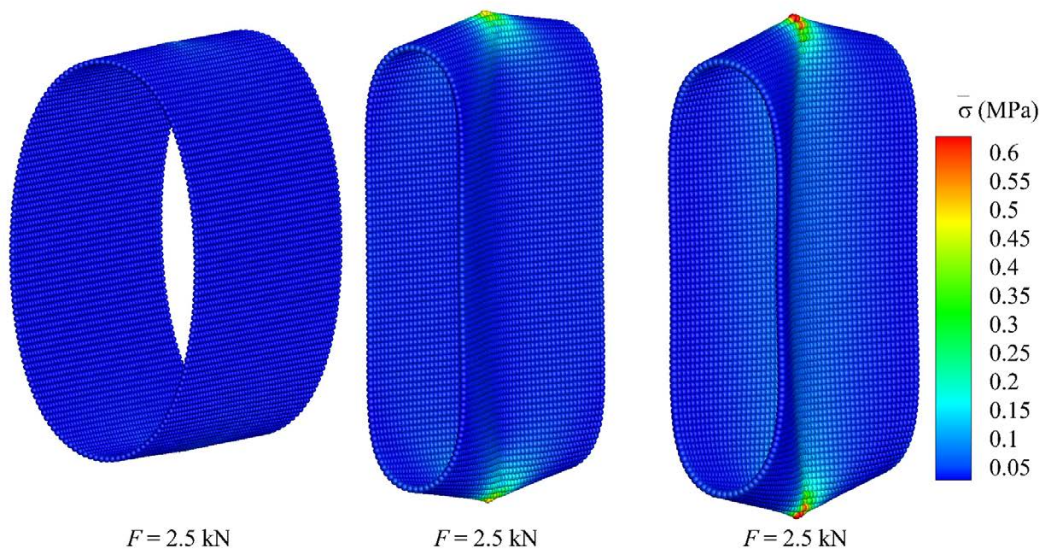


Figure 22: Pulled-out cylindrical shell: Particles colored by the von Mises stress $\bar{\sigma}$ of the mid-surface under 3 point force magnitudes at spatial resolution of $b/dp = 240$. The material parameters are set as the density $\rho_0 = 1100 \text{ kg/m}^3$, Young's modulus $E = 10.5 \text{ MPa}$ and Poisson's ratio $\nu = 0.3125$.

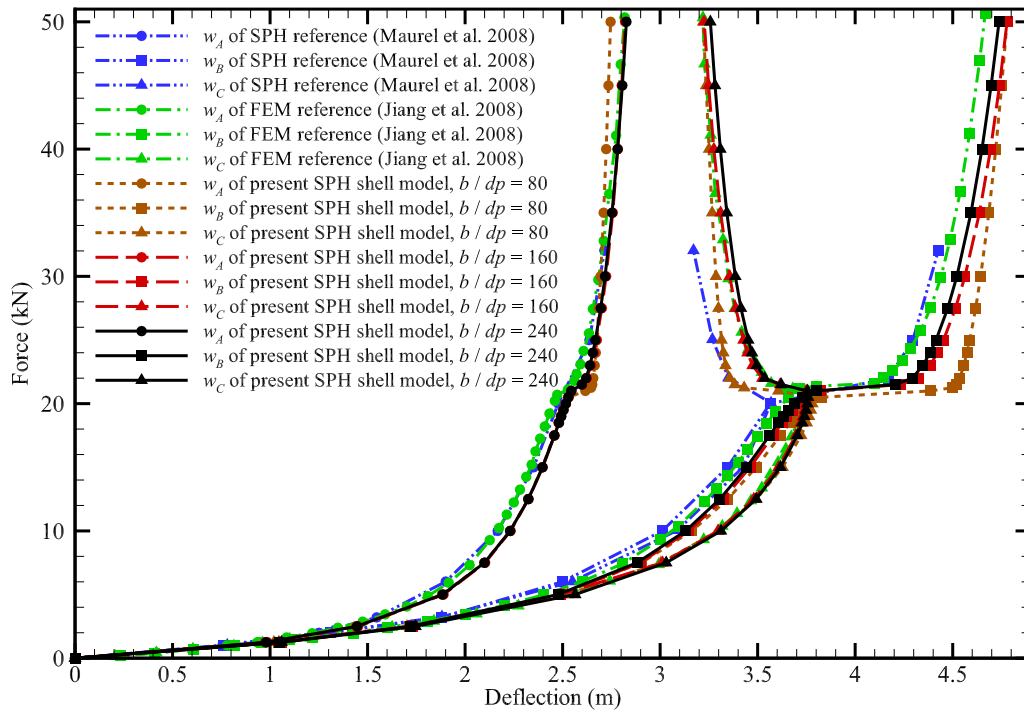


Figure 23: Pulled-out cylindrical shell: Curves of radical displacements of points A , B and C as a function of the point force magnitude and spatial resolution, and their comparison with those of Maurel and Combescure [29] and Jiang et al. [64].

accuracy and robustness of the present method.

4.8. Pinched semi-cylindrical shell

We further consider a pinched semi-cylindrical shell with finite deformation and rotation following Refs. [65, 66, 57, 67]. As shown in Figure 24(a), the semi-cylindrical shell with the radius $r = 1.016$ m, length $a = 3.048$ m and thickness $d = 0.03$ m is completely clamped at a circumferential periphery and experiences a pinching force at the center of free-hanging periphery. Along its longitudinal edges, the vertical direction and the rotation about the y -axis are constrained. The elastic material properties are density $\rho_0 = 1100$ kg/m³, Young's modulus $E = 20.685$ MPa and Poisson's ratio $\nu = 0.3$.

Figure 24(b-d) shows the distribution of von Mises stress $\bar{\sigma}$ at the mid-surface under varying magnitude of the point force \mathbf{F} . Noted that the present method features regular particle distribution and smooth stress fields, even close to the constrained edges and place where the point force is applied, without singularities for finite rotations (more than 0.5π). For quantitative analysis and convergence study, the downward deflection w_A of monitoring point A as a function of the point force magnitude and resolution is compared with that of Ref. [57]. Three different spatial discretizations, i.e., $\pi r/dp = 20, 40$ and 80 , are considered for convergence study. As shown in Figure 25, the result difference obtained by the present SPH shell method between different resolution rapidly decreases as the spatial refinement, and the results agree well with those of Ref. [57].

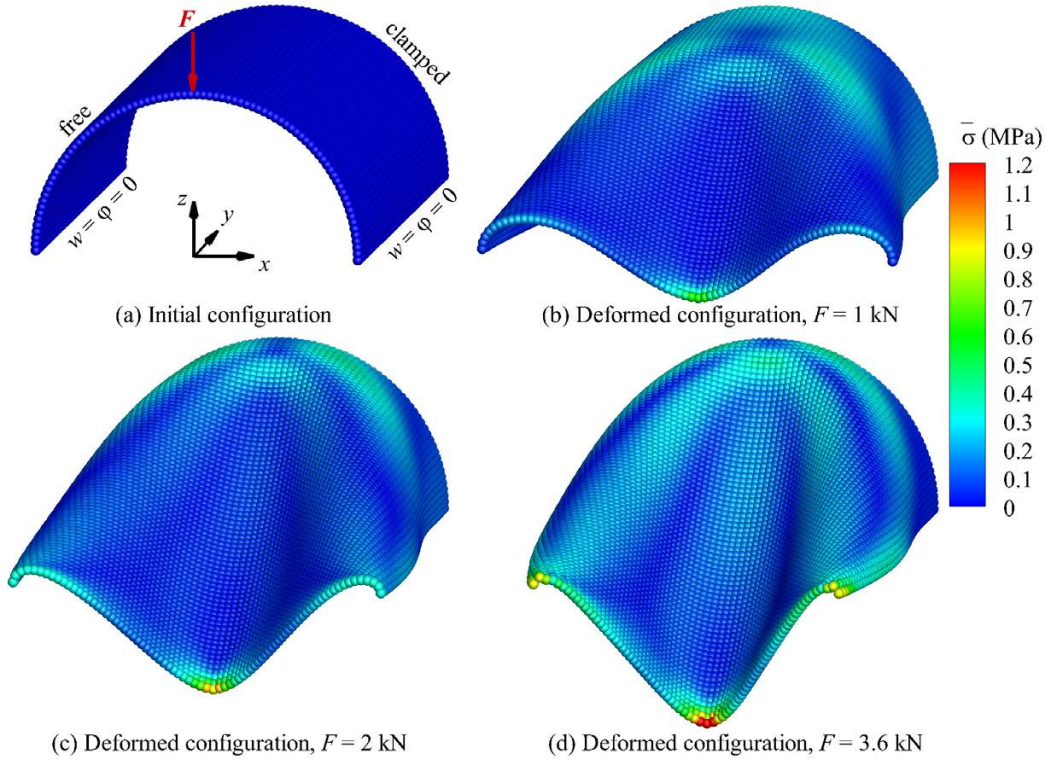


Figure 24: Pinched semi-cylindrical shell: (a) Initial configuration with the radius $r = 1.016$ m, length $a = 3.048$ m and thickness $d = 0.03$ m, (b-d) particles colored by the von Mises stress $\bar{\sigma}$ of the mid-surface under 3 point force magnitudes at spatial resolution $b/dp = 80$. The material parameters are set as the density $\rho_0 = 1100$ kg/m³, Young's modulus $E = 20.685$ MPa and Poisson's ratio $\nu = 0.3$.

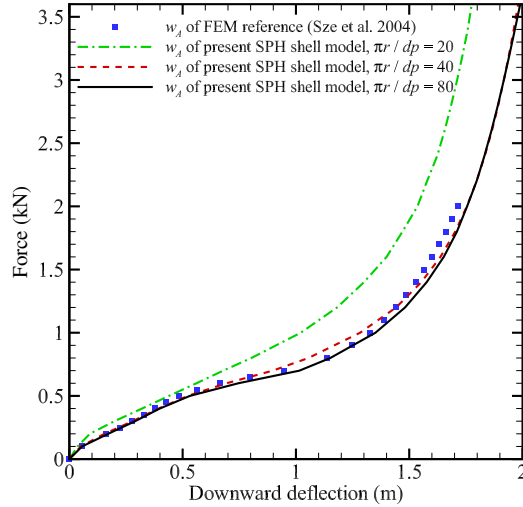


Figure 25: Pinched semi-cylindrical shell: Curves of radical displacements of point A as a function of the point force magnitude and spatial resolution, and their comparison with those of Sze et al. [57].

5. Concluding remarks

In this paper, we present a reduced-dimensional SPH method for quasi-static and dynamic analyses of both thin and moderately thick plate and shell structures. By introducing two reduced-dimensional linear-reproducing correction matrices, the method reproduces linear gradients of the position and pseudo-normal. The finite deformation is taken into account by considering all terms of strain with the help of Gauss-Legendre quadrature along the thickness. To cope with large rotations, the method introduces weighted non-singularity conversion relation between the rotation angles and pseudo normal. A non-isotropic Kelvin-Voigt damping and a momentum-conserving hourglass control algorithm with a limiter are also proposed to increase numerical stability and to suppress hourglass modes. An extensive set of nu-

merical examples have been investigated to demonstrate the accuracy and robustness of the present method. Note that, while the plate and shell structure considered here have moderate and high modulus, one extension of the present method is for soft thin structures, such as membranes. Another outlook, along with the multi-physical modeling within unified computational framework, is to develop the SPH method for the interaction between fluid and thin structures.

CRedit authorship contribution statement

Dong Wu: Conceptualization, Methodology, Investigation, Visualization, Validation, Formal analysis, Writing - original draft, Writing - review & editing; **Chi Zhang:** Investigation, Writing - review & editing; **Xiangyu Hu:** Supervision, Methodology, Investigation, Writing - review & editing.

Declaration of competing interest

The authors declare that they have no known competing financial interests or personal relationships that could have appeared to influence the work reported in this paper.

Acknowledgment

D. Wu is partially supported by the China Scholarship Council (No. 201906130189). D. Wu, C. Zhang and X.Y. Hu would like to express their gratitude to the German Research Foundation (DFG) for its sponsorship of this research under grant number DFG HU1527/12-4.

References

- [1] T. Belytschko, Y. Krongauz, D. Organ, M. Fleming, P. Krysl, Meshless methods: an overview and recent developments, *Computer Methods in Applied Mechanics and Engineering* 139 (1-4) (1996) 3–47.
- [2] G. R. Liu, Y. T. Gu, *An introduction to meshfree methods and their programming*, Springer Science & Business Media, 2005.
- [3] M. Liu, G. Liu, Smoothed particle hydrodynamics (SPH): an overview and recent developments, *Archives of Computational Methods in Engineering* 17 (1) (2010) 25–76.
- [4] C. Zhang, Y.-j. Zhu, D. Wu, N. A. Adams, X. Hu, Smoothed particle hydrodynamics: Methodology development and recent achievement, *Journal of Hydrodynamics* 34 (5) (2022) 767–805.
- [5] L. B. Lucy, A numerical approach to the testing of the fission hypothesis, *The Astronomical Journal* 82 (1977) 1013–1024.
- [6] R. A. Gingold, J. J. Monaghan, Smoothed particle hydrodynamics: theory and application to non-spherical stars, *Monthly Notices of the Royal Astronomical Society* 181 (3) (1977) 375–389.
- [7] J. J. Monaghan, Smoothed particle hydrodynamics, *Reports on Progress in Physics* 68 (8) (2005) 1703.
- [8] J. J. Monaghan, Smoothed particle hydrodynamics and its diverse applications, *Annual Review of Fluid Mechanics* 44 (2012) 323–346.
- [9] C. Zhang, M. Rezavand, Y. Zhu, Y. Yu, D. Wu, W. Zhang, J. Wang, X. Hu, SPHinXsys: An open-source multi-physics and multi-resolution library based

- on smoothed particle hydrodynamics, *Computer Physics Communications* (2021) 108066.
- [10] H. G. Matthies, J. Steindorf, Partitioned strong coupling algorithms for fluid–structure interaction, *Computers & structures* 81 (8-11) (2003) 805–812.
- [11] H. G. Matthies, R. Niekamp, J. Steindorf, Algorithms for strong coupling procedures, *Computer Methods in Applied Mechanics and Engineering* 195 (17-18) (2006) 2028–2049.
- [12] B. C. Cerik, K. Lee, S.-J. Park, J. Choung, Simulation of ship collision and grounding damage using Hosford-Coulomb fracture model for shell elements, *Ocean Engineering* 173 (2019) 415–432.
- [13] Y.-X. Peng, A.-M. Zhang, F.-R. Ming, S.-P. Wang, A meshfree framework for the numerical simulation of elasto-plasticity deformation of ship structure, *Ocean Engineering* 192 (2019) 106507.
- [14] G. Totaro, Z. Gürdal, Optimal design of composite lattice shell structures for aerospace applications, *Aerospace Science and Technology* 13 (4-5) (2009) 157–164.
- [15] J. D. Laubrie, J. S. Mousavi, S. Avril, A new finite-element shell model for arterial growth and remodeling after stent implantation, *International Journal for Numerical Methods in Biomedical Engineering* 36 (1) (2020) e3282.
- [16] P. W. Cleary, Modelling confined multi-material heat and mass flows using SPH, *Applied Mathematical Modelling* 22 (12) (1998) 981–993.
- [17] A. E. H. Love, The Small Free Vibrations and Deformation of a Thin Elastic Shell, *Proceedings of the Royal Society of London Series I* 43 (1887) 352–353.

- [18] Y. S. Uflyand, Wave Propagation by Transverse Vibrations of Beams and Plates, *PMM: Journal of Applied Mathematics and Mechanics* 12 (1948) 287–300.
- [19] R. Mindlin, Influence of rotatory inertia and shear on flexural motions of isotropic, elastic plates, *Journal of Applied Mechanics* 18 (1951) 31–38.
- [20] I. Elishakoff, F. Hache, N. Challamel, Vibrations of asymptotically and variationally based Uflyand–Mindlin plate models, *International Journal of Engineering Science* 116 (2017) 58–73.
- [21] I. Elishakoff, *Handbook on Timoshenko-Ehrenfest beam and Uflyand-Mindlin plate theories*, World Scientific, 2020.
- [22] P. Krysl, T. Belytschko, Analysis of thin shells by the element-free Galerkin method, *International Journal of Solids and Structures* 33 (20-22) (1996) 3057–3080.
- [23] S. Li, W. Hao, W. K. Liu, Numerical simulations of large deformation of thin shell structures using meshfree methods, *Computational Mechanics* 25 (2000) 102–116.
- [24] T. Rabczuk, P. Areias, T. Belytschko, A meshfree thin shell method for non-linear dynamic fracture, *International Journal for Numerical Methods in Engineering* 72 (5) (2007) 524–548.
- [25] D. Li, Z. Lin, S. Li, Numerical analysis of Mindlin shell by meshless local Petrov-Galerkin method, *Acta Mechanica Solida Sinica* 21 (2) (2008) 160–169.

- [26] B. M. Donning, W. K. Liu, Meshless methods for shear-deformable beams and plates, *Computer Methods in Applied Mechanics and Engineering* 152 (1-2) (1998) 47–71.
- [27] J.-S. Chen, D. Wang, A constrained reproducing kernel particle formulation for shear deformable shell in Cartesian coordinates, *International Journal for Numerical Methods in Engineering* 68 (2) (2006) 151–172.
- [28] Y. Peng, A. Zhang, F. Ming, A thick shell model based on reproducing kernel particle method and its application in geometrically nonlinear analysis, *Computational Mechanics* 62 (2018) 309–321.
- [29] B. Maurel, A. Combescure, An SPH shell formulation for plasticity and fracture analysis in explicit dynamics, *International Journal for Numerical Methods in Engineering* 76 (7) (2008) 949–971.
- [30] G. C. Ganzenmüller, An hourglass control algorithm for Lagrangian smooth particle hydrodynamics, *Computer Methods in Applied Mechanics and Engineering* 286 (2015) 87–106.
- [31] D. Wu, C. Zhang, X. Tang, X. Hu, An essentially non-hourglass formulation for total Lagrangian smoothed particle hydrodynamics, *Computer Methods in Applied Mechanics and Engineering* 407 (2023) 115915.
- [32] F.-R. Ming, A.-M. Zhang, X.-Y. Cao, A robust shell element in meshfree SPH method, *Acta Mechanica Sinica* 29 (2) (2013) 241–255.
- [33] F. Caleyron, A. Combescure, V. Faucher, S. Potapov, Dynamic simulation of damage-fracture transition in smoothed particles hydrodynamics shells, *International Journal for Numerical Methods in Engineering* 90 (6) (2012) 707–738.

- [34] J. Lin, H. Naceur, D. Coutellier, A. Laksimi, Efficient meshless SPH method for the numerical modeling of thick shell structures undergoing large deformations, *International Journal of Non-Linear Mechanics* 65 (2014) 1–13.
- [35] F. Ming, A. Zhang, S. Wang, Smoothed particle hydrodynamics for the linear and nonlinear analyses of elastoplastic damage and fracture of shell, *International Journal of Applied Mechanics* 7 (02) (2015) 1550032.
- [36] C. Zhang, Y. Zhu, Y. Yu, D. Wu, M. Rezavand, S. Shao, X. Hu, An artificial damping method for total Lagrangian SPH method with application in biomechanics, *Engineering Analysis with Boundary Elements* 143 (2022) 1–13.
- [37] M. Kondo, Y. Suzuki, S. Koshizuka, Suppressing local particle oscillations in the Hamiltonian particle method for elasticity, *International Journal for Numerical Methods in Engineering* 81 (12) (2010) 1514–1528.
- [38] C. Zhang, M. Rezavand, Y. Zhu, Y. Yu, D. Wu, W. Zhang, S. Zhang, J. Wang, X. Hu, SPHinXsys: An open-source meshless, multi-resolution and multi-physics library, *Software Impacts* 6 (2020) 100033.
- [39] J.-L. Batoz, G. Dhatt, *Modélisation des structures par éléments finis: Solides élastiques*, Presses Université Laval, 1990.
- [40] K. Wisniewski, *Finite rotation shells: Basic equations and finite elements for Reissner kinematics*, CIMNE-Springer, 2010.
- [41] A. Gil, J. Segura, N. M. Temme, *Numerical methods for special functions*, SIAM, 2007.
- [42] J. N. Reddy, *Theory and analysis of elastic plates and shells*, CRC press, 2006.

- [43] H. Wendland, Piecewise polynomial, positive definite and compactly supported radial functions of minimal degree, *Adv. Comput. Math.* 4 (1) (1995) 389–396.
- [44] P. Randles, L. D. Libersky, Smoothed particle hydrodynamics: some recent improvements and applications, *Computer Methods in Applied Mechanics and Engineering* 139 (1-4) (1996) 375–408.
- [45] R. Vignjevic, J. R. Reveles, J. Campbell, SPH in a total Lagrangian formalism, *CMC-Tech Science Press-* 4 (3) (2006) 181.
- [46] P. Betsch, A. Menzel, E. Stein, On the parametrization of finite rotations in computational mechanics: A classification of concepts with application to smooth shells, *Computer Methods in Applied Mechanics and Engineering* 155 (3-4) (1998) 273–305.
- [47] J. C. Simo, D. D. Fox, M. S. Rifai, On a stress resultant geometrically exact shell model. Part III: Computational aspects of the nonlinear theory, *Computer Methods in Applied Mechanics and Engineering* 79 (1) (1990) 21–70.
- [48] P. Singla, D. Mortari, J. L. Junkins, How to avoid singularity for Euler angle set, in: *Proceedings of the AAS Space Flight Mechanics Conference, Hawaii, 2004*, pp. AAS04–190.
- [49] T. J. Hughes, K. S. Pister, Consistent linearization in mechanics of solids and structures, *Computers & Structures* 8 (3-4) (1978) 391–397.
- [50] C. Zhang, M. Rezavand, X. Hu, A multi-resolution SPH method for fluid-structure interactions, *Journal of Computational Physics* 429 (2021) 110028.
- [51] T. Y. Tsui, P. Tong, Stability of transient solution of moderately thick plate by finite-difference method, *AIAA journal* 9 (10) (1971) 2062–2063.

- [52] L. D. Landau, E. M. Lifchits, Course of theoretical physics: Theory of elasticity (1986).
- [53] J. P. Gray, J. J. Monaghan, R. Swift, SPH elastic dynamics, *Computer Methods in Applied Mechanics and Engineering* 190 (49-50) (2001) 6641–6662.
- [54] C. Zhang, X. Y. Hu, N. A. Adams, A generalized transport-velocity formulation for smoothed particle hydrodynamics, *Journal of Computational Physics* 337 (2017) 216–232.
- [55] B. Momenan, M. R. Labrosse, A New Continuum-Based Thick Shell Finite Element for Soft Biological Tissues in Dynamics: Part 1-Preliminary Benchmarking Using Classic Verification Experiments, *arXiv preprint arXiv:1801.04029* (2018).
- [56] K. Sze, S.-J. Zheng, A stabilized hybrid-stress solid element for geometrically nonlinear homogeneous and laminated shell analyses, *Computer Methods in Applied Mechanics and Engineering* 191 (17-18) (2002) 1945–1966.
- [57] K. Sze, X. Liu, S. Lo, Popular benchmark problems for geometric nonlinear analysis of shells, *Finite Elements in Analysis and Design* 40 (11) (2004) 1551–1569.
- [58] G. Payette, J. Reddy, A seven-parameter spectral/hp finite element formulation for isotropic, laminated composite and functionally graded shell structures, *Computer Methods in Applied Mechanics and Engineering* 278 (2014) 664–704.
- [59] T. Belytschko, H. Stolarski, W. K. Liu, N. Carpenter, J. S. Ong, Stress projection for membrane and shear locking in shell finite elements, *Computer Methods in Applied Mechanics and Engineering* 51 (1-3) (1985) 221–258.

- [60] J. Simo, D. Fox, M. Rifai, On a stress resultant geometrically exact shell model. Part II: The linear theory; computational aspects, *Computer Methods in Applied Mechanics and Engineering* 73 (1) (1989) 53–92.
- [61] J. Simo, M. Rifai, D. Fox, On a stress resultant geometrically exact shell model. Part IV: Variable thickness shells with through-the-thickness stretching, *Computer Methods in Applied Mechanics and Engineering* 81 (1) (1990) 91–126.
- [62] N. Buechter, E. Ramm, Shell theory versus degeneration—a comparison in large rotation finite element analysis, *International Journal for Numerical Methods in Engineering* 34 (1) (1992) 39–59.
- [63] L. Jiang, M. Chernuka, A simple four-noded corotational shell element for arbitrarily large rotations, *Computers & structures* 53 (5) (1994) 1123–1132.
- [64] L. Jiang, M. W. Chernuka, N. G. Pegg, A co-rotational, updated Lagrangian formulation for geometrically nonlinear finite element analysis of shell structures, *Finite Elements in Analysis and design* 18 (1-3) (1994) 129–140.
- [65] N. Stander, A. Matzenmiller, E. Ramm, An assessment of assumed strain methods in finite rotation shell analysis, *Engineering Computations* 6 (1) (1989) 58–66.
- [66] B. Brank, F. Damjanić, D. Perić, On implementation of a nonlinear four node shell finite element for thin multilayered elastic shells, *Computational Mechanics* 16 (5) (1995) 341–359.
- [67] R. Arciniega, J. Reddy, Tensor-based finite element formulation for geometrically nonlinear analysis of shell structures, *Computer Methods in Applied Mechanics and Engineering* 196 (4-6) (2007) 1048–1073.